

VHE gamma-ray intranight variability from BL Lacertae during the extreme flaring state of 2022

K. Abe¹, S. Abe², A. Abhishek³, F. Acero^{4,5}, A. Aguasca-Cabot⁶, I. Agudo⁷, C. Alispach⁸, D. Ambrosino⁹, F. Ambrosino¹⁰, L. A. Antonelli¹⁰, C. Aramo⁹, A. Arbet-Engels¹¹, C. Arcaro¹², T.T.H. Arnesen¹³, P. Aubert¹⁴, A. Baktash¹⁵, M. Balbo⁸, A. Bamba¹⁶, A. Baquero Larriva^{17,18}, U. Barres de Almeida¹⁹, J. A. Barrio¹⁷, L. Barrios Jiménez¹³, I. Batkovic¹², J. Baxter², J. Becerra González¹³, J. Bernete²⁰, A. Berti¹¹, E. Bissaldi²¹, O. Blanch²², G. Bonnoli²³, P. Bordas⁶, A. Briscioli²⁴, G. Brunelli^{25,26}, J. Bucés¹⁷, A. Bulgarelli²⁵, I. Burelli²⁷, L. Burmistrov²⁸, M. Cardillo²⁹, S. Caroff¹⁴, A. Carosi¹⁰, R. Carraro¹⁰, F. Cassol²⁴, D. Cerasole^{30*}, A. Cerviño Cortínez¹⁷, Y. Chai¹¹, G. Chon¹¹, L. Chytka³¹, G. M. Cicciari^{32,33}, J. L. Contreras¹⁷, J. Cortina²⁰, H. Costantini²⁴, M. Croisnonnier²², M. Dalchenko²⁸, G. D'Amico²², P. Da Vela²⁵, F. Dazzi¹⁰, A. De Angelis¹², M. de Bony de Lavergne³⁴, R. Del Burgo⁹, C. Delgado²⁰, J. Delgado Mengual³⁵, D. della Volpe²⁸, B. De Lotto²⁷, L. Del Peral³⁶, R. de Menezes¹⁹, G. De Palma²¹, V. de Souza³⁸, C. Díaz²⁰, L. Di Bella³⁹, A. Di Piano²⁵, F. Di Pierro³⁷, R. Di Tria³⁰, L. Di Venere⁴⁰, D. Dominis Prester⁴¹, A. Donini¹⁰, D. Dorner⁴², L. Eisenberger⁴², D. Elsässer³⁹, G. Emery^{7*}, L. Felgion²⁴, F. Ferrarotto⁴³, A. Fiasson^{14,44}, L. Foffano²⁹, Y. Fukazawa⁴⁵, S. Gallozzi¹⁰, R. García López¹³, S. García Soto²⁰, C. Gasbarra⁴⁶, D. Gasparrini⁴⁶, J. Giesbrecht Paiva¹⁹, N. Giglietto²¹, F. Giordano³⁰, N. Godinovic⁴⁷, T. Gradetzke³⁹, R. Grau²², J. Green¹¹, G. Grolleron¹⁴, S. Gunji⁴⁸, P. Günther⁴², J. Hackfeld⁴⁹, D. Hadasch⁵⁰, M. Hashizume⁴⁵, T. Hassan²⁰, K. Hayashi^{2,51}, L. Heckmann^{11,52}, M. Heller²⁸, J. Herrera Llorente¹³, N. Hiroshima², D. Hoffmann²⁴, D. Horns¹⁵, J. Houles²⁴, D. Hrupec⁵³, R. Imazawa⁴⁵, T. Inada², S. Inoue^{2,54}, K. Ioka⁵⁵, M. Iori⁴³, T. Itokawa², A. Iuliano⁹, J. Jahanvi²⁷, I. Jimenez Martinez¹¹, J. Jimenez Quiles²², I. Jorge Rodrigo²⁰, J. Jurysek⁵⁶, M. Kagaya^{2,51}, V. Karas⁵⁷, H. Katagiri⁵⁸, D. Kerszberg^{22,59}, T. Kiyomoto⁶⁰, Y. Kobayashi², K. Kohri⁶¹, P. Kornecki⁷, H. Kubo², J. Kushida¹, B. Lacave²⁸, M. Lainez¹⁷, A. Lamastra¹⁰, L. Lemoigne¹⁴, M. Linhoff³⁹, S. Lombardi¹⁰, F. Longo⁶², R. López-Coto⁷, A. López-Oramas¹³, S. Loporchio³⁰, J. Lozano Bahilo³⁶, F. Lucarelli¹⁰, H. Luciani⁶², P. L. Luque-Escamilla⁶³, M. Makariev⁶⁴, M. Mallamaci^{32,33}, D. Mandat⁵⁶, K. Mannheim⁴², F. Marini¹², M. Mariotti¹², P. Marquez⁶⁵, G. Marsella^{32,33}, J. Martí⁶³, O. Martínez^{66,67}, G. Martínez²⁰, M. Martínez²², M. Massa³, D. Mazin^{2,11}, J. Méndez-Gallego⁷, S. Menon^{10,68}, E. Mestre Guillen⁶⁹, D. Miceli¹², T. Miener¹⁷, J. M. Miranda⁶⁶, M. Molero Gonzalez¹³, E. Molina¹³, T. Montaruli²⁸, A. Moralejo²², A. Morselli⁴⁶, V. Moya¹⁷, A. L. Müller⁵⁶, H. Muraishi⁷⁰, S. Nagataki⁷¹, T. Nakamori⁴⁸, A. Neronov⁷², D. Nieto Castaño¹⁷, M. Nieves Rosillo¹³, L. Nikolic³, K. Noda^{2,54}, V. Novotny⁷³, S. Nozaki², M. Ohishi², Y. Ohtani², A. Okumura^{74,75}, R. Orito⁷⁶, L. Orsini⁷⁷, J. Otero-Santos^{12*}, P. Ottanelli⁷⁷, M. Palatiello¹⁰, G. Panebianco²⁵, D. Paneque¹¹, R. Paoletti³, J. M. Paredes⁶, M. Pech^{31,56}, M. Pecimotika²², M. Peresano¹¹, F. Perrotta⁷⁸, F. Pfeifle⁴², M. Pihet⁶, G. Pirola¹¹, C. Plard¹⁴, F. Podobnik³, M. Polo²⁰, C. Pozo-González⁷, E. Prandini¹², S. Rainò³⁰, R. Rando¹², W. Rhode³⁹, M. Ribó⁶, G. Rodríguez Fernández⁴⁶, M. D. Rodríguez Frías³⁶, A. Roy⁴⁵, A. Ruina¹², E. Ruiz-Velasco¹⁴, T. Saito², S. Sakurai², D. A. Sanchez¹⁴, H. Sano^{2,79}, E. Santos Moura³⁸, T. Šarić⁴⁷, Y. Sato⁸⁰, F. G. Saturni¹⁰, V. Savchenko⁷², F. Schiavone³⁰, F. Schussler³⁴, T. Schweizer¹¹, M. Seglar Arroyo²², G. Silvestri¹², A. Simongini^{10,68}, J. Sitarek⁸¹, V. Sliusar⁸, I. Sofia³⁷, J. Striškovici⁵³, M. Strzys², Y. Suda⁴⁵, A. Sunny^{10,68}, H. Tajima⁷⁴, M. Takahashi⁷⁴, R. Takeishi², S. J. Tanaka⁸⁰, D. Tateishi⁶⁰, T. Tavernier⁵⁶, P. Temnikov⁶⁴, Y. Terada⁶⁰, K. Terauchi⁸², T. Terzić⁴¹, M. Teshima^{2,11}, M. Tluczykont¹⁵, T. Tomura², D. F. Torres⁵⁰, F. Tramonti³, P. Travnicek³⁶, G. Tripodo³³, A. Tutone¹⁰, M. Vacula³¹, M. Vázquez Acosta¹³, G. Verna³, I. Viale¹², A. Viana³⁸, A. Vigliano²⁷, C. F. Vigorito^{37,83}, E. Visentin^{37,83}, V. Vitale⁴⁶, G. Voutsinas²⁸, I. Vovk², T. Vuillaume¹⁴, R. Walter⁸, T. Yamamoto⁸⁴, R. Yamazaki⁸⁰, Y. Yao¹, T. Yoshida⁵⁸, T. Yoshikoshi², W. Zhang⁵⁰, N. Zywuca⁸¹ (the CTAO-LST collaboration), F. Aceituno⁷, J. A. Acosta-Pulido¹³, V. Casanova⁷, J. Escudero Pedrosa⁷, J. Jormanainen⁴⁵, S. Jorstad⁸⁵, G. Keating⁸⁶, P. M. Kouch⁴⁵, M. Gurwell⁸⁶, A. Lähteenmäki^{87,88}, E. Lindfors⁴⁵, A. Marscher⁸⁵, D. Morcuende^{7*}, I. Myserlis^{89,90}, K. Nilsson⁴⁵, C. A. Ortega Hunter⁷, R. Rao⁸⁶, A. Sota⁷, M. Tornikoski⁹⁰, and H. Zhang^{91,92}

(Affiliations can be found after the references)

Received October 31, 2025; accepted March 18, 2026

ABSTRACT

Context. BL Lacertae (BL Lac), the archetype blazar of its subclass and one of the most studied blazars in the last decades, has gone through a series of major multi-wavelength outbursts since 2020, resulting in its highest recorded γ -ray flare up to date between September and November 2022 together with those from August 2021 and October 2024.

Aims. We characterise the γ -ray and multi-wavelength emission and spectral energy distribution (SED) of BL Lac, as well as their evolution during the major and extended γ -ray and multi-wavelength flare occurring between September and November 2022.

Methods. We evaluate the variability of the flare, with focus on the nights of October 20 and November 13, when clear intranight very-high-energy (VHE, $E > 100$ GeV) γ -ray variability is observed. We model the γ -ray and broadband SEDs during periods of stable emission identified with a Bayesian block analysis, interpreting their evolution of the flare from the variability of the relativistic particles and physical parameters of the jet.

Results. The VHE emission shows an average flux of 0.23 Crab Units (C.U.) above 200 GeV during this flare and a variability amplitude of more than a factor 10. Intranight doubling-flux variations as fast as ~ 8 minutes are observed during the nights of October 20 and November 13, when maximum fluxes of 4.4 C.U. above 100 GeV and 2.8 C.U. above 200 GeV are reached. The spectral analysis reveals a transition of the X-ray emission from the high- to the low-energy SED peak, and a shift of the γ -ray peak towards higher energies. The broadband emission was interpreted within a leptonic two-zone model in which intranight variability is explained as magnetic reconnection in a compact region closely oriented with the line of sight, while weekly-scale variations can be explained as variations of the relativistic electron distributions and the injection of freshly accelerated particles.

Key words. Galaxies: active – BL Lacertae objects: general – BL Lacertae objects: individual: BL Lacertae – Galaxies: jets – Galaxies: nuclei – gamma rays: galaxies

1. Introduction

Relativistic jets launched from blazars — active galactic nuclei (AGN) with their jets oriented towards our line of sight — are known to be extremely efficient and natural particle accelerators, which are able to emit in all the electromagnetic spectrum. In fact, they are one of the few sources that can emit up to TeV energies. Blazars are also highly variable on all timescales. Depending on the properties of their optical spectrum (absence/presence of broad emission lines, see [Stickel et al. 1991](#)), they can be classified into two main sub-classes: BL Lac type objects and flat spectrum radio quasars (FSRQs) ([Urry & Padovani 1995](#)).

The broadband spectral energy distribution (SED) of blazars, extending from radio to γ -ray energies, has a characteristic double-peak shape. The low-energy component is produced by synchrotron radiation (see [Konigl 1981](#)). The invoked mechanisms behind the high-energy component fall in two groups. An interpretation based on leptonic processes explains this emission through Inverse Compton (IC) scattering with low-energy photons, either synchrotron radiation via synchrotron self Compton (SSC, see [Konigl 1981](#); [Maraschi et al. 1992](#)) scattering, or with radiation from outside the jet via External Compton (EC, see [Dermer & Schlickeiser 1994](#)) scattering. However, interpretations based on a hadronic nature are also used in some cases, relying on processes like proton synchrotron radiation or photopion production to explain the high-energy emission of blazars (see e.g. [Mannheim & Biermann 1992](#); [Aharonian 2000](#)).

BL Lacertae (hereafter BL Lac), the archetype of the BL Lac blazar subclass located at redshift $z = 0.069$ ([Miller et al. 1978](#)), has historically shown remarkable variability with several episodes of minute- to hour-scale variations (see for instance [Abeysekara et al. 2018](#); [MAGIC Collaboration et al. 2019](#); [Jorstad et al. 2022](#)), becoming one of the most monitored and studied blazars over the years. It is classified as an intermediate-synchrotron-peaked (ISP) blazar according to the peak frequency of its synchrotron emission ($10^{14} \text{ Hz} < \nu_{\text{syn}} < 10^{15} \text{ Hz}$). However, it is known for transitioning between the low-synchrotron-peaked (LSP, $\nu_{\text{syn}} < 10^{14} \text{ Hz}$) and ISP types, depending on its activity (see e.g. [Ackermann et al. 2011](#); [Nilsson et al. 2018](#)). It has been detected several times in the very-high-energy (VHE, $E > 100 \text{ GeV}$) γ -ray band, always during multi-wavelength flaring emission states ([Albert et al. 2007](#); [Arlen et al. 2013](#)). These periods of variability on very short timescales imply very compact emitting regions involving the most energetic particle acceleration processes, and challenging in some cases the theoretical models used for interpreting the broadband emission of blazars ([Henri & Saugé 2006](#)).

Here we report the results of an extreme flare observed from BL Lac by the Large-Sized Telescope prototype (LST-1), taking place between September and November 2022, and triggered after the detection of enhanced activity by the *Fermi* satellite ([La Mura 2022](#)). This flare is one of the three brightest events ever detected in VHEs from BL Lac, together with similar events occurring in 2021 and 2024, and it is also the most long-lasting flaring period ever recorded for this source in the VHE domain, lasting for about 3 months, with significant variations in day, hour and minute timescales. This remarkable flare was also covered by several multi-wavelength facilities, providing a rich dataset for interpreting the multi-wavelength emission and variability of BL Lac in this period (see Sect. 2). In this work, we evaluate and interpret the VHE γ -ray and broadband evolution of

the flare. We characterise the minute-scale γ -ray variability observed during this period (Sect. 3), that sets important constraints to the nature of the emitting region. The spectral behaviour of the source is evaluated (Sect. 4), and its broadband emission is modelled within AGN radiative models (Sect. 5). The main results are discussed and summarised in Sects. 6 and 7.

2. Observations and data reduction

2.1. VHE γ -ray data: LST-1

LST-1 is the first of the four Large-Sized Telescopes that will be constructed in the northern site of the Cherenkov Telescope Array Observatory (CTAO, [Acharyya et al. 2019](#)) at the Roque de los Muchachos Observatory in the Canary Island of La Palma (Spain). LST-1 is currently performing commissioning and scientific observations, after the completion of its construction in October 2018. Its large collection area (23 m diameter mirror) and very sensitive camera — composed of 1855 high quantum efficiency photomultiplier tubes — allow to detect faint Cherenkov light flashes from γ -ray showers down to energies $\approx 20 \text{ GeV}$ (see [Abe et al. 2023](#)).

LST-1 observed BL Lac for 23 nights between September 21 and November 25, 2022 in wobble observing mode ([Fomin et al. 1994](#)), providing ~ 36 hours of data after applying standard data quality cuts in a zenith range between 10° and 60° . The analysis of the raw LST-1 data was performed with version v0.10.18 of the `cta-lstchain` software ([López-Coto et al. 2022](#); [Moralejo et al. 2025](#)), including data cleaning, image parametrisation, γ -hadron separation and direction and energy reconstruction of the recorded events. Among this dataset, ~ 29 hours of data were taken under dark sky conditions (no increased background light contamination due to the presence of the moon) with a standard tail-cut cleaning with thresholds of 8 and 4 photoelectrons (p.e.) for the core and neighbour pixels of the Cherenkov shower image and an intensity cut of 50 p.e. ([Abe et al. 2023](#)). The remaining ~ 7 hours of observation were performed with different moon brightness levels. These data were analysed with cleaning thresholds ranging from 10 to 16 p.e. and 5 to 8 p.e. for the core and neighbour pixels, and increased intensity cuts between 63 and 194 p.e. due to the noise introduced by the moon, extracted from the data at each night sky background (NSB) level. The event classification was performed with a Random Forest trained using Monte Carlo (MC) simulated proton- and γ -like events at a declination of 34.74° , close to that of BL Lac (42.28°). The MCs were produced to match the NSB level of our data, accounting for the additional noise with respect to dark observations. For the event selection, energy-dependent gammaness (gamma-likeness score) and θ (angular distance of the detected event with respect to the nominal source position) cuts were used, optimised to preserve 70% of the simulated MC γ -ray events.

The high level analysis was done with version 1.2 of `Gammapy` ([Donath et al. 2023](#); [Aguasca-Cabot et al. 2023](#); [Acero et al. 2024](#)). The background was characterised using an OFF region with a wobble angle of 0.4° and at a reflected position of 180° from that of BL Lac. A limit on the effective area $A_{\text{eff}} > 5\%$ of the maximum area was also applied. The statistical significance was calculated following Eq. (17) from [Li & Ma \(1983\)](#). The energy threshold of the light curve, calculated from the maximum of the distribution of expected events from the MCs, weighted with BL Lac's spectrum, with the highest NSB level and zenith distance between 40° and 50° to match that of the data, was estimated to be $\sim 175 \text{ GeV}$. Therefore, we have used a minimum energy of 200 GeV for the light curve reconstruction.

* Corresponding authors (in alphabetical order): D. Cerasole, G. Emery, D. Morcuende, J. Otero-Santos; email: lst-contact@cta-observatory.org

The energy threshold was further verified on data against background asymmetries in the field of view (FoV). We observed a non-uniformity of the event distribution, in particular along the altitude axis. This effect increases when the telescope pointing is further from the zenith, and becomes clearly visible at zenith distances $>40^\circ$. Looking at the energy distribution of events in the source region and the OFF region, a clear difference in energy threshold is visible for some observations. While the difference seems mostly at energies below our analysis threshold, we also perform our spectral analysis using backgrounds counts estimation using the package `BACcMod`¹. This package allows to extract the background distribution using the full FoV after removing the source region and can thus account for asymmetries. As expected, we observe differences in the extracted spectra below 200 GeV for some time periods, but the spectra agree above 200 GeV thus validating our results above this energy. The VHE γ -ray light curve is shown in the top panel of Fig. 1. We highlight October 20 and November 13 as two remarkably bright nights, when significances of $\sim 49\sigma$ and $\sim 30\sigma$ were reached in only 2.5 and 1.5 hours of observation. The minute-scale variability of these two nights is evaluated in Sect. 3. In particular for October 20, consisting only of dark-sky data, we adopted a threshold of 100 GeV obtained from the dark-sky MCs with zenith ~ 20 – 40° . The spectrum and SED were characterised with a log-parabola model plus a term accounting for the Extragalactic Background Light (EBL) absorption with the model from [Saldana-Lopez et al. \(2021\)](#). The spectral analysis is presented in detail in Sect. 4.

2.2. HE γ -ray data: Fermi-LAT

We also analysed high-energy (HE, $E > 100$ MeV) data taken by the pair-conversion Large Area Telescope (LAT) on board the *Fermi* satellite. The LAT operates in sky-survey mode in an energy range between 20 MeV and ~ 1 TeV, with its best sensitivity around a few GeV ([Atwood et al. 2009](#)). We considered a 20° -radius region of interest (ROI) centred at the position of BL Lac. All data from September 21 to November 30 were downloaded, selecting the `Pass8 P8R3_SOURCE_V3` events between 100 MeV and 300 GeV with the `FERMITOOLS` standard software. A zenith angle cut of 90° was applied to minimise the contamination from the limb of the Earth. Furthermore, we used the recommended versions of the Galactic diffuse emission model and isotropic component for the event selection considered².

To account for the emission of sources nearby BL Lac, we derived a model including all sources within the ROI, plus all sources located in an additional annular region of radius 10° . This model was constructed using 1 year of data and a binned likelihood analysis procedure, using as reference the 4FGL-DR2 catalogue ([Abdollahi et al. 2020](#); [Ballet et al. 2020](#)). The spectral parameters (index and normalisation) of all variable sources — as defined in the 4FGL catalogue based on the LAT variability index — contained in the ROI and with a Test Statistics (TS, [Mattox et al. 1996](#)) >25 ($\sim 5\sigma$ significance) were left as free parameters, while those not fulfilling these conditions were fixed to the catalogue values. The normalisation of the diffuse components was also left free. Convergence to the final model was achieved after removing all sources with $TS < 4$ ($< 2\sigma$).

The HE γ -ray light curve was then obtained analysing the data within the desired time window through an unbinned likeli-

hood analysis of events contained in 12-hour bins. For each bin we have assumed a power law spectral shape for BL Lac, leaving the spectral index and the normalisation free. The spectral parameters of the rest of the sources were fixed to the values from the model, with the exception of two highly variable and bright sources with a significant detection ($TS > 25$) located at a distance $< 15^\circ$ from BL Lac (4FGL J2244.2+4057 and 4FGL J2311.0+3425). The HE γ -ray light curve is shown in Fig. 1.

2.3. X-ray data: Swift-XRT

The scientific payload onboard the *Neil Gehrels Swift* observatory includes by the X-Ray Telescope (XRT, [Burrows et al. 2005](#)), and the Optical/UV Telescope (UVOT, [Roming et al. 2005](#)). In standard operation mode, these instruments perform simultaneous observations on the same targets. In this project, we included 50 *Swift*-XRT and *Swift*-UVOT observations on BL Lac carried out since March 2022 up to January 2023.

Swift-XRT is sensitive to X-rays in the 0.2 – 10 keV energy range. The reduced XRT data were downloaded from the UK Swift Science Data Center ([Evans et al. 2009](#)). The spectral analysis on the reduced data was performed using the `XSPEC v12.13.1` package through `PyXspec v2.1.2`. We analysed the XRT data in the energy range from 0.3 to 10 keV. The intrinsic source emission in this range was primarily modelled with a power-law function and, to test the presence of intrinsic spectral curvature related to the transition between the synchrotron and IC bumps, with a log-parabola model. The observed spectra were fitted with the intrinsic emission models folded with the `tbabs`³ Galactic absorption term, as implemented in `XSPEC`. Following [Raiteri et al. \(2009\)](#), in the fit procedures we fixed the neutral hydrogen column density toward BL Lac to $n_H = 3.4 \times 10^{21} \text{ cm}^{-2}$ and we employed this value to correct the X-ray fluxes and SEDs for the Galactic extinction effects. The F -test was employed to assess whether the log-parabola model was preferred over the power-law one, with a 3σ significance level cut. The results of the X-ray analysis are summarised in Appendix B.

2.4. Ultraviolet data: Swift-UVOT

The analysis of UVOT data was carried out using the `uvotimsum` and `uvotsource` tasks within the `HEASOFT 6.32` package, along with the latest (v20240201) *Swift*/UVOT Calibration Database (CALDB) files. UVOT performed photometric observations on BL Lac using the optical *vv*, *bb*, *uu* and UV *w1*, *m2*, *w2* filters ([Poole et al. 2008](#)). Through `uvotsource`, we estimated the observed fluxes in the UVOT filters using a circular source region with radius of $5''$ centred on BL Lac and a circular background region with a $10''$ radius in a nearby region devoid of sources. The observed fluxes were corrected for Galactic extinction effects using $E(B-V) = 0.2802 \pm 0.0119$ ([Schlafly & Finkbeiner 2011](#)) using the standard procedure described in [Fitzpatrick \(1999\)](#). Moreover, the contributions of the host galaxy in the UVOT photometric filters *vv*, *bb*, *uu*, *w1*, *m2*, *w2*, given the adopted aperture, were estimated as 2.89, 1.30, 0.36, 0.026, 0.020, and 0.017 mJy, respectively ([Raiteri et al. 2013](#)). Both host galaxy contributions and Galactic extinction effects were accounted for to reconstruct the intrinsic BL Lac spectral points in the optical-UV band. The results of the analysis of the *Swift*-UVOT data from the 2022 high state are reported in Table C.1.

¹ <https://github.com/mdebony/BACcMod>

² <https://fermi.gsfc.nasa.gov/ssc/data/access/lat/BackgroundModels.html>

³ <https://heasarc.gsfc.nasa.gov/xanadu/xspec/manual/node273.html>

2.5. Optical data

Optical observations in the *BVRI* Johnson-Cousins bands were taken by the Sierra Nevada Observatory (SNO) as part of the TOP-MAPCAT photo-polarimetric blazar monitoring programme (Agudo et al. 2012). The data were reduced with the IOP4 software (Escudero Pedrosa et al. 2024a,b). Observations in the *R* band were also performed as part of the Tuorla blazar monitoring⁴ with the 80 cm Joan Oró Telescope at Montsec Astronomical Observatory (Spain), reduced as detailed in Nilsson et al. (2018). Data in the *BVRI* bands were taken by the IAC80 telescope at the Teide Observatory. Finally, observations with the robotic telescope network of Las Cumbres Observatory (Brown et al. 2013) were also coordinated in the *RV* optical bands.

Additionally, data from the public all-sky survey programmes and databases All-Sky Automated Survey for Supernovae (ASAS-SN, Shappee et al. 2014; Kochanek et al. 2017) in the Sloan *g* band, and Zwicky Transient Facility (ZTF, Bellm et al. 2019) in the Sloan *gr* bands, were also included. These Sloan magnitudes were converted into the Johnson-Cousins photometric system using the transformations from Lupton (2005)⁵.

The contribution of the host galaxy emission to the total observed optical emission contained in the employed aperture has been subtracted (see Raiteri et al. 2009). Moreover, all data have been corrected from the reddening effect introduced by the Galactic extinction. For this, we adopt the extinction values $A_B = 1.192$, $A_V = 0.901$, $A_R = 0.713$ and $A_I = 0.495$ reported by Schlafly & Finkbeiner (2011). The optical flux density light curves are presented in Fig. 1.

2.6. Radio-millimetric data

Observations in the 37-GHz radio band were performed with the 13.7-m diameter Metsähovi radio telescope as part of its long-term AGN monitoring⁶ (Terasranta et al. 1998). Additionally, we compiled five observations in the 225-GHz band performed with the Submillimeter Array (SMA, Ho et al. 2004) at Mauna Kea, Hawaii. SMA is an 8-element 6-meter diameter dish radio interferometer with two orthogonally polarised receivers, allowing us to measure the total and the polarised flux of astrophysical objects. These receivers are inherently linearly polarised, however they can be converted to circular thanks to quarter-wave plates installed on the polarimeter (Marrone & Rao 2008). These observations were carried out by the SMA Monitoring of AGNs with Polarisation (SMAPOL) programme (Myserlis et al. 2025), dedicated to the regular monitoring of γ -ray loud blazars, including BL Lac, on a bi-weekly cadence. The data were calibrated with the MIR⁷ package following standard procedures.

3. VHE intranight variability

In addition to the day-to-week variability, we have evaluated the VHE γ -ray intranight variability, a feature less often observed in blazars (other examples are e.g. Aharonian et al. 2007; MAGIC Collaboration et al. 2020). Its detection presents significant constraints to the emitting region size and the interpretation of the emission, potentially favouring leptonic models as hadrons usually require longer times for being accelerated and have longer

cooling times by a factor $\sim (m_p/m_e)^3$. We evaluate the nights with the highest VHE γ -ray flux, October 20 and November 13. The 5-minute binned light curves are shown in Fig. 2.

3.1. October 20th flare

We have evaluated the fastest variability timescales observed during the night of October 20. For this night we consider the integrated flux above an energy of 100 GeV, as all the data were taken under dark-sky conditions and zenith distances ~ 20 – 40° . As shown in the left panel of Fig. 2, the rise and decay of the flare is well sampled by the LST-1 data, varying from ~ 1.0 C.U. to ~ 4.4 C.U. in ~ 1 – 1.5 hours. This well defined rise and decay profile of the flare during this night enabled us to model the light curve as a rising and decaying exponential function, commonly used for modelling light curves (Norris et al. 1996) including those from blazar flares (see e.g. Aharonian et al. 2007),

$$F(t) = F_b + \begin{cases} F_0 e^{-(t_{peak}-t)/t_r} & : t < t_{peak}; \\ F_0 e^{-(t-t_{peak})/t_d} & : t > t_{peak}; \end{cases} \quad (1)$$

where F_0 represents the flux of the flare at a time t_{peak} , F_b is the baseline flux that we have fixed at $(0.45 \pm 0.09) \times 10^{-9} \text{ cm}^{-2} \text{ s}^{-1}$, obtained from the stable bins at the beginning and end of the flare, and t_r and t_d are the timescales of the flare rise and decay variations by a factor of e . We have modelled the 5-minute binned light curve of October 20 as a sum of three possible substructures during the development of the flare with peak values found at $t_{max,1} = 35.0 \pm 4.8$ min, $t_{max,2} = 75.0 \pm 3.7$ min and $t_{max,3} = 105.0 \pm 8.2$ min, considering the first flux point as $t_0 = 0$ min. We note that we have also considered the simpler cases of one or two components, comparing the goodness of the fit in each case. We measure $\chi^2/\text{d.o.f.}$ values for the triple-, double- and single-exponential profiles of 18.0/22, 42.6/25 and 54.5/28, which yields a significance of the triple-exponential model over the double- and single-function of 4.2σ and 4.7σ , respectively, using Wilks theorem (Wilks 1938). We also checked that the light curve modelling does not improve adding a fourth component, with a preference over the three-component one of 0.2σ . Therefore, we adopted the model based on the sum of three exponential profiles defined by Eq. (1).

The fitted function is shown in the left panel of Fig. 2, and the calculated rise and decay timescales of exponential profile are reported in Table 1. These timescales can be used to estimate the doubling flux variability timescale during the rise and decay, representative of the fastest significant variability timescales, as

$$\tau_{rise/fall} = t_{r/d} \times \ln(2). \quad (2)$$

With this approach we are able to resolve variability timescales of ~ 18 min with a confidence level of $>5\sigma$, and faster hints of between 2.2 min and 4.6 min, however with a significance $\leq 2\sigma$.

Alternatively, we can also estimate the fastest variability timescales through the doubling time criterion considering flux variations between consecutive temporal bins, following the procedure from Zhang et al. (1999) as

$$t_{doubling,i} = \frac{F_i + F_{i+1}}{2} \frac{t_{i+1} - t_i}{|F_{i+1} - F_i|}, \quad (3)$$

where F_{i+1} and F_i are the fluxes at times t_{i+1} and t_i . We consider only those timescales obtained through this method for which the significance of the variability is $>2\sigma$. The results derived with this approach are reported in the last column of Table 1. We observe significant doubling flux timescales of $\tau_{min} = 8.3 \pm 2.5$ min.

⁴ <https://tuorlablazar.utu.fi/>

⁵ <https://classic.sdss.org/dr4/algorithms/sdssUBVRITransform.php#Lupton2005>

⁶ <https://www.aalto.fi/en/metsahovi-radio-observatory/active-galaxies>

⁷ <https://lweb.cfa.harvard.edu/~cqi/mircook.html>

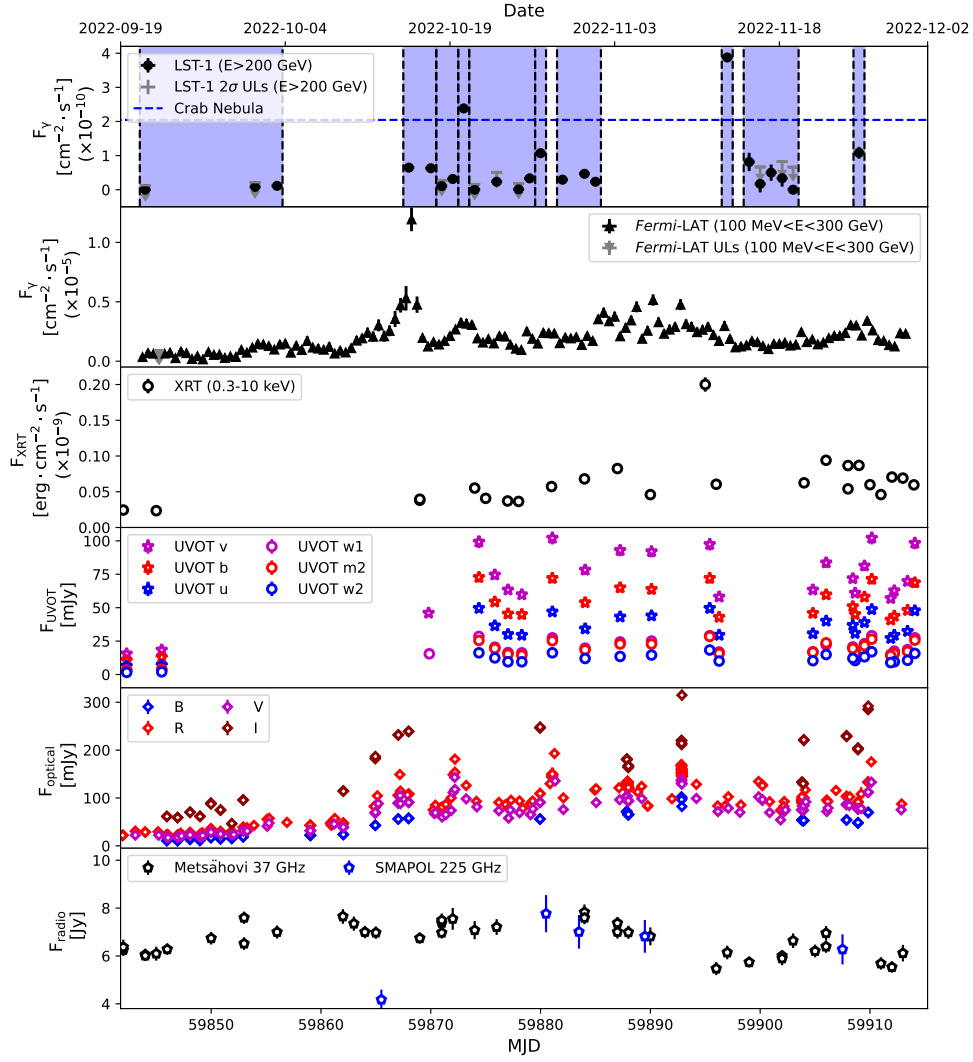


Fig. 1. Multi-wavelength light curves of BL Lacertae between September 21 and November 30, 2022. *From top to bottom:* LST-1 night-wise VHE γ -ray light curve above 200 GeV, *Fermi*-LAT 12-hour binned HE γ -ray light curves between 100 MeV and 300 GeV, XRT X-ray light curve between 0.3 and 10 keV, UVOT optical-UV light curves in the different filters available, optical light curves in the *BVRI* bands, 37-GHz and 225-GHz radio light curves. The blue dashed line in the top panel corresponds to the Crab Nebula flux above 200 GeV (Aleksić et al. 2016). The blue contours delimited by black dashed lines highlight the Bayesian blocks identified in the LST-1 light curve.

Table 1. Results of the VHE γ -ray intranight variability analysis, reporting the shortest variability timescales derived from the rise and decay light curve modelling and doubling flux criterion.

Date	F_b [$10^{-9} \times \text{cm}^{-2} \text{s}^{-1}$]	F_0 [$10^{-9} \times \text{cm}^{-2} \text{s}^{-1}$]	t_{max} [min]	t_r [min]	t_d [min]	τ_{rise} [min]	τ_{fall} [min]	$t_{doubling}$ [min]
October 20	0.45 ± 0.09	0.75 ± 0.15	35.0 ± 4.8	3.2 ± 1.8	4.7 ± 2.5	2.2 ± 1.2	3.3 ± 1.7	8.3 ± 2.5
		1.43 ± 0.10	75.0 ± 3.7	26.1 ± 4.7	52.4 ± 7.7	18.1 ± 3.3	36.3 ± 5.3	
November 13	0.27 ± 0.05	0.75 ± 0.25	105.0 ± 8.2	6.1 ± 3.7	6.7 ± 4.2	4.2 ± 2.6	4.6 ± 2.9	–
		0.30 ± 0.04	0	–	28.9 ± 5.9	–	20.0 ± 4.1	

Applying causality arguments, it is expected that very fast variability originates in very compact jet regions. Therefore, the fastest variability timescales observed can be used to constrain the size of the emitting region responsible for such variations as

$$R \leq \frac{\tau_{min} c \delta}{1 + z}, \quad (4)$$

where R is the radius of the emitting region, τ_{min} represents the fastest variability timescale observed, c is the speed of light, δ is the Doppler factor of the region and z corresponds to the

redshift of the source (see Dondi & Ghisellini 1995; Tavecchio et al. 2010). Here we adopt a conservative approach, using the shortest timescale with a significance $>3\sigma$ before trials, this is, $\tau_{min} = 8.3 \pm 2.5$ min. With this timescale, and considering a range of Doppler factor values $\delta = 10 - 50$, the size of the emitting region responsible for the fast variability must be $R \leq (1.4 \pm 0.4) \times 10^{14}$ cm to $R \leq (7.0 \pm 2.1) \times 10^{14}$ cm. We note that if the 2.2- to 6.7-minute timescales are confirmed, this would imply a region a factor ~ 1.5 to ~ 4 more compact. Nevertheless, in addition to the low significance, when considering the

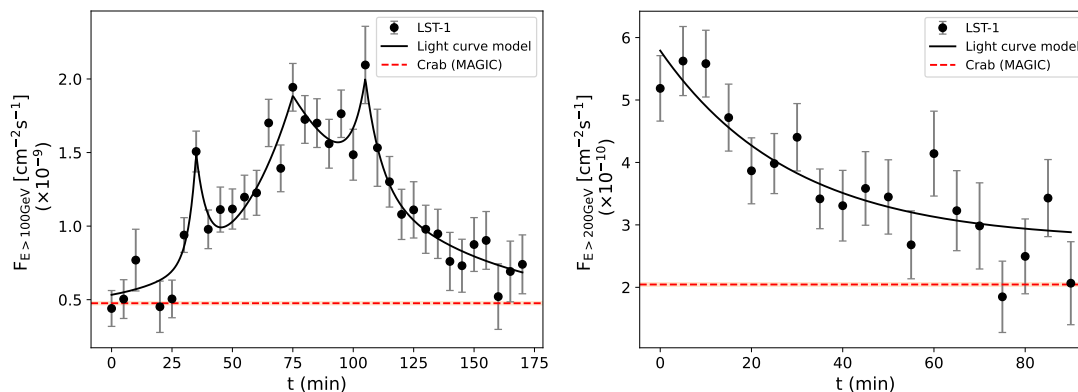


Fig. 2. Intranight light curves of BL Lac. *Left:* 5-minute binned light curve during the night of October 20 above 100 GeV. *Right:* 5-minute binned light curve during the night of November 13 above 200 GeV. Black points correspond to LST-1’s measurements. Black solid lines represent the light curve models. The horizontal dashed red lines show the flux of the Crab Nebula as measured by the MAGIC telescopes (Aleksić et al. 2016).

typical systematic errors for LST-1 flux measurements (see Abe et al. 2023), these timescales get hindered within uncertainties.

3.2. November 13th flare

The same analysis was performed for the night of November 13, when we also observed intranight variability in the VHE γ -ray emission of BL Lac. In this case, and owing to the higher energy threshold introduced by the moon conditions, we consider the flux above 200 GeV. During this night, the emission decayed from ~ 2.8 C.U. to ~ 1.0 C.U. in 1.5 hours. The corresponding 5-minute binned light curve is shown in the right panel of Fig. 2. In this case, LST-1 covered only the decay of the VHE γ -ray flare, that we modelled with a decaying exponential function as

$$F(t) = F_b + F_0 e^{-(t_{\text{peak}} - t)/t_d}, \quad (5)$$

that follows the same description as Eq. (1). A value of $(0.27 \pm 0.05) \times 10^{-9} \text{ cm}^{-2} \text{ s}^{-1}$ was used for F_b , where the VHE flux seems to stabilise after the flare. The results for this night are reported as well in Table 1. With the estimated timescale $\tau_{\text{min}} = 20.0 \pm 4.1$ min, we have again constrained the size of the emitting region with Eq. (4), for typical Doppler factors $\delta = 10 - 50$. This leads to a size constraint ranging from $R \leq (3.4 \pm 0.7) \times 10^{14}$ cm to $R \leq (16.8 \pm 3.5) \times 10^{14}$ cm. We note that in this case, the doubling flux criterion does not find significant minute-scale variability.

4. Characterisation of the HE-VHE γ -ray spectrum

In order to evaluate possible γ -ray spectral variability patterns, we have studied the evolution of the γ -ray spectrum during the flare. For this, we have applied a Bayesian Block (BB) analysis on the VHE γ -ray light curve using the algorithm developed by Wagner et al. (2022)⁸, identifying 10 BBs of comparable γ -ray activity with a false positive rate of 1% (see Fig. 1). Then, making use of the LAT and LST-1 data, we characterise the high-energy SED peak for the different identified periods from 100 MeV up to a few TeV. For this, we perform a joint fit of the data from both instruments with Gammapy, that allows to combine multi-instrument data at an event level, correctly accounting for instrument response functions (IRFs), backgrounds and other effects such as EBL absorption (Nieves Rosillo et al. 2025).

For the *Fermi*-LAT data of each BB, we filter out all sources in the model that have a $\text{TS} < 10$. The parameters of all sources

contained in a circular region of 10° radius centred at the position of BL Lac and with a $\text{TS} > 30$ are left free, while for those sources within 5° from BL Lac with $\text{TS} < 30$, only the spectral normalisation is left as a free parameter. For the remaining sources, all parameters are fixed to the catalogue values. Then, a pre-fit of the *Fermi*-LAT data is performed, allowing to remove weak sources still included in the model for which the number of expected counts is < 5 . Finally, we combine the LAT and LST-1 datasets of each BB and calculate the complete γ -ray spectrum and SED peak, incorporating into the analysis the response of each instrument.

We have tested several spectral shapes of the HE-VHE emission, including log-parabola, power-law with exponential cut-off and log-parabola with exponential cut-off spectral models. We find that the first function provides the most accurate fit to our data. Therefore, we use a model consisting on a log-parabola function plus a term accounting for the EBL absorption at redshift $z = 0.069$ with the model from Saldana-Lopez et al. (2021),

$$\phi(E) = \phi_0 (E/E_0)^{-\alpha - \beta \log(E/E_0)} e^{-\alpha_{\text{EBL}} \tau(E,z)}. \quad (6)$$

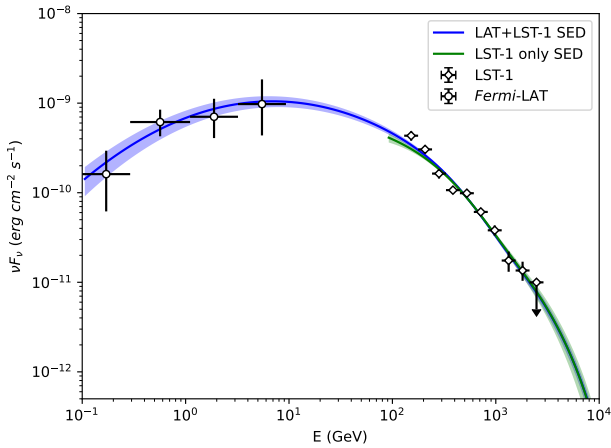
To perform a direct comparison between the different spectra, we adopted an $E_0 = 1$ GeV for all periods. The best-fit spectral parameters are reported in Table 2. In Fig. 3 we show an example of the joint SED for the eighth BB, that is, the night of November 13. The rest of the SEDs are available in Figs. E.1 and E.2. Alternatively, owing to the very small variability in the spectral curvature, we tested a log-parabola function fixing $\beta = 0.12$, taken from the average value over the entire period. The results were consistent within uncertainties with those reported in Table 2.

The complete characterisation of the high-energy SED peak performed in Sect 4 allows us to search for spectral variability patterns during the evolution of the flare. We observe a relatively stable value of the spectral index at 1 GeV around $\alpha \sim 1.90$, with almost all BBs consistent within errors at a $\sim 2\sigma$ level. Nevertheless, spectral index variations are particularly noticeable for the nights of October 20 with $\alpha = 1.53$, and November 13 with $\alpha = 1.56$, meaning that during these flares, particles are being accelerated to much higher energies. This is also visible from the high-energy peak shift, reported in Table 2. The IC peak shift becomes evident for the four brightest BBs, this is, the nights of October 20 and 27, and November 13 and 25, being the only ones with $E_{\text{peak}} > 2$ GeV. The average value of E_{peak} is found below 2 GeV, and during these nights we observe shifts up to values of

⁸ <https://github.com/swagner-astro/lightcurves>

Table 2. Results of the joint LAT and LST-1 γ -ray intrinsic SED spectrum at an energy $E_0 = 1$ GeV after correcting by EBL absorption for each BB.

	Period [MJD]	f_0 [GeV ⁻¹ cm ⁻² s ⁻¹]	α	β	E_{peak} [GeV]	νF_{ν}^{max} [erg cm ⁻² s ⁻¹]
BB1	59843.5 – 59856.5	$(6.68 \pm 0.58) \times 10^{-8}$	1.92 ± 0.07	0.13 ± 0.02	1.4	$(1.09 \pm 0.11) \times 10^{-10}$
BB2	59867.5 – 59870.5	$(2.86 \pm 0.50) \times 10^{-7}$	1.86 ± 0.08	0.10 ± 0.01	1.9	$(4.81 \pm 0.85) \times 10^{-10}$
BB3	59870.5 – 59872.5	$(2.41 \pm 0.46) \times 10^{-7}$	1.80 ± 0.13	0.14 ± 0.03	1.9	$(4.14 \pm 0.90) \times 10^{-10}$
BB4	59872.5 – 59873.5	$(4.66 \pm 0.86) \times 10^{-7}$	1.53 ± 0.06	0.14 ± 0.01	5.5	$(1.11 \pm 0.12) \times 10^{-9}$
BB5	59873.5 – 59879.5	$(1.97 \pm 0.16) \times 10^{-7}$	1.99 ± 0.06	0.13 ± 0.02	1.1	$(3.15 \pm 0.27) \times 10^{-10}$
BB6	59879.5 – 59880.5	$(2.62 \pm 0.24) \times 10^{-7}$	1.81 ± 0.08	0.11 ± 0.01	2.3	$(4.58 \pm 0.45) \times 10^{-10}$
BB7	59881.5 – 59885.5	$(3.03 \pm 0.18) \times 10^{-7}$	1.91 ± 0.04	0.11 ± 0.01	1.6	$(4.95 \pm 0.35) \times 10^{-10}$
BB8	59896.5 – 59897.5	$(4.26 \pm 0.88) \times 10^{-7}$	1.56 ± 0.07	0.11 ± 0.01	6.5	$(1.05 \pm 0.15) \times 10^{-9}$
BB9	59898.5 – 59903.5	$(1.71 \pm 0.12) \times 10^{-7}$	1.86 ± 0.05	0.11 ± 0.01	1.9	$(2.86 \pm 0.24) \times 10^{-10}$
BB10	59908.5 – 59909.5	$(3.48 \pm 0.30) \times 10^{-7}$	1.84 ± 0.05	0.10 ± 0.01	2.3	$(5.94 \pm 0.62) \times 10^{-10}$


Fig. 3. Joint LAT-LST-1 SED for BB8 using a log-parabola plus EBL model. White circles and squares correspond to the LAT and LST-1 spectral points, respectively. Down-pointing arrows correspond to flux upper limits. The blue and red lines and bowtie shapes represent the best fits of the joint LAT+LST-1 and LST-1-only data, respectively.

5.5 GeV for October 20, 6.5 GeV for November 13, and 2.3 GeV for October 27 and November 25. The Spearman correlation coefficient between E_{peak} and α , and E_{peak} and f_0 show a high level of correlation ($\rho \sim 0.85$ and $\rho \sim 0.75$, respectively), indicating a possible harder-when-brighter behaviour. However, this correlation coefficient is dominated by the two brightest nights and does not account for uncertainties.

5. Broadband SEDs

We have modelled the evolution of the broadband emission of BL Lac during the 2022 high state. We have considered 10 broadband SEDs, corresponding to each of the BBs identified above. Fig. 4 shows as an example the model for the eighth BB. All fitted SED models are presented in Figs. F.1 and F.2. We note that, due to the lack of strictly simultaneous *Swift* data (± 0.5 days with respect to the LST-1 observations) to BBs 3, 4, 6, 8 and 9, for these periods we have considered a window of ± 1.5 days in order to have complete multi-wavelength coverage of the SEDs.

We have considered a leptonic-only origin for the broadband emission. We use version v0.4.0 of the PYTHON package *agnpy* (Nigro et al. 2022; Nigro et al. 2023). We find that SSC models based on a single emitting region are not able to accurately describe the broadband emission of BL Lac during this period. One-zone models based on EC scattering rise as an alternative to

explain the VHE γ -ray emission, and have actually been invoked in the past for BL Lac due to the presence of a small and weak broad line region (BLR), using its external low-energy photons as seeds for the γ -ray production (MAGIC Collaboration et al. 2019). However, this solution was also found to be insufficient in this case to reproduce the broadband emission and variability during the 2022 high state, especially given the tight constraints on the emitting region size set by the intranight variability. Therefore, we consider a SSC model based on two emitting regions (Tavecchio et al. 2011), which has been used frequently to model the multi-wavelength emission of this source (see e.g. MAGIC Collaboration et al. 2019; Sahakyan & Giommi 2022). We denote the two regions as "core" and "blob", with sizes $R_{core} > R_{blob}$. We consider the regions to be co-spatial and interacting. This is motivated by the high correlation of the broadband emission from the optical band up to γ rays (Appendix D.2). A scheme of this layout is illustrated in Fig. 9b of MAGIC Collaboration et al. (2019). Each region is defined by a magnetic field B , a Lorentz factor Γ , a Doppler factor δ and an electron population that we have characterised through a broken power-law distribution with respect to the electron Lorentz factor γ ,

$$N(\gamma) = \begin{cases} K(\gamma/\gamma_b)^{-n_1} & : \gamma_{min} < \gamma < \gamma_b \\ K(\gamma/\gamma_b)^{-n_2} & : \gamma_b < \gamma < \gamma_{max} \end{cases} \quad (7)$$

where K is the normalisation of the distribution, γ_{min} and γ_{max} are the minimum and maximum values of the Lorentz factor, and n_1 and n_2 are the spectral indices below and above the break of the distribution γ_b , respectively. We constrain the size of the blob, responsible for the intranight VHE γ -ray variability, with the estimates presented in Sect. 3. Additionally, we have incorporated to the SED model an EC contribution from external photon fields, namely the BLR, the accretion disc and the dusty torus. This is because, as mentioned above, these components have been used in the past to reproduce the large width of the IC SED peak (see e.g. Khatoon et al. 2024). Following Ghisellini & Tavecchio (2009); MAGIC Collaboration et al. (2019), we adopt $L_{BLR} = 2.5 \times 10^{42}$ erg s⁻¹ and $R_{BLR} = 2 \times 10^{16}$ cm for the BLR, which leads to $L_{disc} = 2.5 \times 10^{43}$ erg s⁻¹ and $R_{torus} = 4 \times 10^{17}$ cm using the typical relations between BLR, disc and torus (see Kaspi et al. 2007; Cleary et al. 2007), assuming in this case a covering factor for torus of $\Xi_{DT} = 0.1$, and a BLR reprocessing factor (based on the H α line) $\xi_{H\alpha} = 0.1$. For the dusty torus, we assumed a typical temperature of 1000 K. We adopted a black hole mass of $M_{BH} = 10^{8.7} M_{\odot}$ (Ghisellini et al. 2010). Finally, we considered the core located at a distance $d_{core} = 6.5 \times 10^{17}$ cm from the central engine and the blob at

Table 3. SED modelling parameters for the two-zone SSC model describing the broadband emission during each BB.

(1)	(2)	(3)	(4)	(5)	(6)	(7)	(8)	(9)	(10)	(11)	(12)	(13)	(14)
Epoch	Component	γ_{\min} ($\times 10^3$)	γ_b ($\times 10^4$)	γ_{\max} ($\times 10^5$)	n_1	n_2	B [G]	K [$\times 10^{-2} \text{ cm}^{-3}$]	R [$\times 10^{15} \text{ cm}$]	Γ	δ	U'_B/U'_e	t_{SSC} [min]
BB1	Blob	3.00	0.90	0.17	2.0	2.8	0.50	3.00	0.3	33	33	0.31×10^{-2}	35.0
	Core	0.27	0.20	0.05	2.2	3.4	0.20	0.01	100	20	20	1.64	–
BB2	Blob	2.50	1.00	1.50	2.8	3.8	0.50	3.00	0.3	33	33	0.13×10^{-2}	15.3
	Core	0.30	0.23	0.05	1.9	2.9	0.20	0.01	100	20	20	1.54	–
BB3	Blob	3.00	0.95	0.80	2.9	3.7	0.50	3.00	0.3	33	33	0.17×10^{-2}	19.2
	Core	0.25	0.23	0.05	2.0	2.9	0.20	0.01	100	20	20	0.75	–
BB4	Blob	2.50	0.95	1.80	2.6	3.5	0.50	5.00	0.3	33	33	0.11×10^{-2}	11.1
	Core	0.30	0.19	0.07	2.0	2.8	0.20	0.01	100	20	20	2.00	–
BB5	Blob	3.20	1.00	0.35	2.8	3.8	0.50	3.00	0.3	33	33	0.17×10^{-2}	17.9
	Core	0.25	0.20	0.07	2.4	3.4	0.20	0.01	100	20	20	0.79	–
BB6	Blob	2.00	0.95	1.10	2.7	3.4	0.50	3.00	0.3	33	33	0.13×10^{-2}	16.2
	Core	0.50	0.25	0.07	2.4	3.7	0.20	0.01	100	20	20	0.88	–
BB7	Blob	2.70	1.05	1.00	2.7	3.6	0.50	3.00	0.3	33	33	0.13×10^{-2}	12.3
	Core	0.30	0.23	0.07	2.2	3.3	0.20	0.01	100	20	20	1.19	–
BB8	Blob	4.00	1.00	3.80	2.1	3.8	0.50	7.50	0.3	33	33	0.11×10^{-2}	8.8
	Core	0.30	0.18	0.07	1.9	3.0	0.20	0.01	100	20	20	2.56	–
BB9	Blob	3.60	1.00	0.80	2.7	3.6	0.50	3.00	0.3	33	33	0.20×10^{-2}	17.5
	Core	0.15	0.19	0.06	2.3	2.7	0.20	0.01	100	20	20	0.85	–
BB10	Blob	2.00	1.05	1.00	2.6	3.6	0.50	3.00	0.3	33	33	0.11×10^{-2}	12.1
	Core	0.28	0.20	0.06	2.3	3.0	0.20	0.01	100	20	20	1.45	–

Notes. Columns: (1) Observation campaign/state. (2) Emission region. (3), (4) and (5) Minimum, break and maximum electron Lorentz factor. (6) and (7) Electron distribution slopes below and above γ_b . (8) Magnetic field. (9) Electron density. (10) Emission-region size. (11) Bulk Lorentz factor. (12) Doppler factor. (13) Ratio between the magnetic field and the relativistic electrons energy density. (14) Blob SSC cooling time at γ_b .

$d_{blob} = 6.2 \times 10^{17}$ cm. We also take into account the possible $\gamma\gamma$ absorption at GeV-TeV energies and the EBL absorption at VHE. We also evaluated the $\gamma\gamma$ absorption due to the external radiation fields, which was found to be negligible.

Multi-zone models of blazar SEDs are characterised by a high degree of degeneracy, owing to the relatively large number of parameters. This degeneracy generally prevents the use of standard fit routines based on the minimisation of a cost function to effectively constrain the parameter space. In such cases, it is necessary to adopt a physically motivated scenario as guiding framework. In this work, we have investigated a scenario in which the evolution of the flare is driven by magnetic reconnection, which is strongly supported by the minute-scale variability detected at VHE with LST-1. In order to fit the SED of each BB, for each block we have used the parameters of the previous one as initial parameters, iterating until reaching a good representation of the SED. To reduce the number of free parameters, we have kept the magnetic fields B , the emitting region sizes R , the Lorentz factor Γ and the Doppler factor δ fixed (with values in agreement with the limit values set by the variability analysis). Additionally, we minimise the changes of physical parameters in the core region between adjacent BBs to reflect the slow evolving nature of the core, unless the observed time interval between the centre of two adjacent BBs is longer than two days, the light crossing timescale of the core region in our reference frame. The blob, in contrast, is considered as the newly formed plasmoid from an unresolved magnetic reconnection layer in the core, whose parameters can vary considerably depending on the reconnection layer. Therefore, we have based our SED evolution in changes of the electron distribution of each region, that is, K , γ_{\min} , γ_b , γ_{\max} , n_1 and n_2 . The parameter change was done in a way that is consistent with the flare's evolution timescales. The resulting models for each BB are shown in Figs. F.1 and F.2, and the parameters describing each of them are summarised in

Table 3. The consistency of these models with a magnetic reconnection scenario is discussed in Sect. 6.

The leptonic origin of the emission considered here is supported by recent results obtained by the IXPE (Imaging X-ray Polarimetry Explorer) satellite, based on the analysis of the broadband polarised emission of BL Lac (see [Middei et al. 2023](#); [Peirson et al. 2023](#)). Under a leptonic framework where the X-ray spectrum is dominated by the high-energy IC scattering component, the X-ray polarisation degree Π_X is expected to be substantially lower than that of the optical band, which originates from electron synchrotron radiation ([Lioudakis et al. 2019](#); [Peirson & Romani 2019](#); [Zhang et al. 2024](#)). [Middei et al. \(2023\)](#) measured an upper limit of $\Pi_X < 12.6 - 14.2\%$ for two IXPE observations of BL Lac during May and July 2022, consistent with this scenario given the optical polarisation degree.

Moreover, under strong flares where the soft X-ray emission has significant contribution from synchrotron radiation as observed from the much flatter X-ray spectrum — which is also the present case, see for instance BB3 with respect to e.g. BB8 when the source was at its brightest — one expects a significantly higher polarisation degree of the soft X-ray photons than that at hard X-ray energies, and even higher than the optical polarisation degree ([Lioudakis et al. 2019](#); [Peirson & Romani 2019](#); [Zhang et al. 2024](#)). A third IXPE observation of BL Lac, performed two days after the last LST-1 observation (November 27 to 29) resulted in a measured X-ray polarisation degree of $\Pi_X = 27.6\% \pm 11.6\%$ over the entire X-ray band. After splitting the analysis in two bins accounting for the soft and hard X-ray regimes, almost all the polarised emission was found to be in the former, with a polarisation degree of $\Pi_X = 27.6^{+5.6}_{-7.9}\%$. The synchrotron emission was estimated to comprise 44% of the total flux at the soft X-ray band ([Peirson et al. 2023](#)). After accounting only for the synchrotron emission and assuming that the 56% of the flux remaining comes from unpolarised SSC, the X-ray polarisation fraction was calculated to be $\sim 49\%$, much higher than

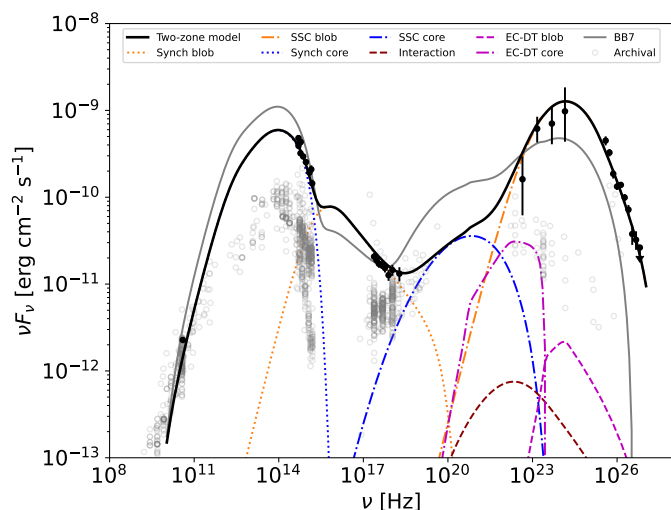


Fig. 4. Broadband SED of BL Lac for BB8. Black points and arrows correspond to flux points and upper limits obtained from the different instruments. The black solid line represents the fitted co-spatial two-zone SSC model. The blue dotted and dashed-dotted lines show the synchrotron and SSC emission of the core, respectively. The orange dotted and dashed-dotted lines indicate the synchrotron and SSC emission of the blob. The magenta dashed-dotted and dashed lines are the EC emission from the core and the blob, respectively. The dark red dashed line is the emission resulting from the interaction between the core and the blob. The grey solid line is the SED of the previous block. The historical data retrieved from the SSDC database (<https://tools.ssdsc.asi.it/SED/>) are shown with grey open points.

that in optical frequencies ($\sim 13\%$), and well within the expectations for a SSC scenario (Peirson & Romani 2019). Therefore, the leptonic SED modelling performed here is consistent with the expected nature of the broadband emission based on both the spectral and the multi-wavelength polarisation analyses.

A last IXPE campaign on BL Lac during November 2023 resulted in an extremely high optical polarisation of 47.5%, not accompanied however with a high X-ray polarisation, leading to a 3σ upper limit of 7.4%. This was observed during a period in which BL Lac was behaving as an LSP. Therefore, the X-ray emission was located in the high-energy SED component. These results strongly favour SSC multi-zone or energy-stratified models (see Zhang et al. 2024; Agudo et al. 2025), leaving little room for hadronic contribution, only in the framework of a hybrid model as shown by a detailed analysis of the broadband emission by Liidakis et al. (2025). However, as presented by these authors, hybrid models expect a hardening of the VHE spectrum that is not observed here in order to reproduce the multi-wavelength polarisation signatures.

6. Discussion

6.1. γ -ray and X-ray spectral behaviour

X-ray spectral trends were also observed in BL Lac prior to the 2022 high state (e.g. Weaver et al. 2020). Through an extensive SED modelling, Sahakyan & Giommi (2022) attributed the synchrotron component emerging in X-rays during periods of high state to a second emission zone located beyond the BLR, different from the one dominating the emission in the optical-UV band. The emission from this second region can produce a shift of the synchrotron peak towards higher frequencies, reaching values of even $\gtrsim 10^{15} - 10^{16}$ Hz, well within the high-

synchrotron-peaked (HSP) range. Indeed, BL Lac is well known for transitioning between the LSP regime — mainly during low flux states — to an IBL/HBL behaviour during active phases (see e.g. Ackermann et al. 2011; Nilsson et al. 2018). Starting on approximately 2019, the source has been going through several years of very high activity, culminating with its three brightest flares ever recorded in 2021, 2022 and 2024. Therefore, the X-ray spectral variability trends observed in the dataset analysed in this work can be related to the emergence of synchrotron emission from freshly accelerated particles in a secondary emission region along the jet. The shift of the X-ray emission from the high- to the low-energy peak of the SED can also be the reason behind the lower correlation of the hard X-ray and optical flux compared to the soft X-ray one, as reported in Appendix D.2. Furthermore, in our model the emission from the secondary region (blob) dominates also in the HE and VHE γ -ray bands. Therefore, the same freshly accelerated particles are also responsible for the intense flaring activity detected with *Fermi*-LAT and LST-1 via SSC, as well as for the observed brightening and shifting of the γ -ray spectrum towards higher energies (see Sect. 4).

6.2. Week-scale evolution of the broadband emission

We successfully model the broadband emission and evolution of the flare as a SSC two-zone model considering as well the EC contribution. The flare begins with emission dominated by the slowly evolving core, extending up to X-ray energies. Plasmoids (blobs) can develop within some considerably magnetised current sheets within the core through magnetic reconnection. These blobs become primarily responsible for the gamma-ray emission. At this early stage of the flare, the EC scattering also contributes to the gamma-ray emission. As magnetic reconnection sets in, particles in the blob are accelerated to higher energies, increasing its contribution also in the X-ray band. Our spectral fitting reveals several major ejections of plasmoids/blobs in the emission region, namely, BB4, BB6, BB8, and BB10. During all these episodes, a freshly produced blob dominates the gamma-ray emission, and can also have strong contributions in other wavelengths depending on the blob parameters. All those episodes are followed by a relatively low flux episode, where the newly formed blob cools and loses its energy. Since each blob is produced independently, their parameters are expected to be considerably different. On the other hand, the core evolves slowly, thus its physical parameters do not change much between different episodes.

This layout is in agreement with the correlation analysis performed in Appendix D.2, where the high degree of correlation between different bands can be attributed to the co-spatial nature of the broadband emission, with the exception of the lower correlation found with the radio and VHE bands. For the former, it is known that the inner regions of the jet are highly opaque to radio emission, that is typically assumed to come from an outer part (Max-Moerbeck et al. 2014). Several studies have in fact found long delays of hundreds of days between the radio and multi-wavelength emission of blazars (see e.g. Liidakis et al. 2018). We cannot test this hypothesis here as we focus on a shorter period. Nevertheless, such behaviour could explain the lower correlation of this band. We note, however, that the radio band as a lower observing cadence than that in optical, that can also be biasing the measured correlation. Regarding the latter band, the lower correlation of the VHE emission can be explained by the shorter cooling timescales of the highest-energy electrons responsible for the TeV emission. However, as for the radio band correlation, the lower observing cadence of the VHE

data can introduce systematic effects in the correlation analysis, diluting the correlation of the TeV emission.

With the configuration assumed in Sect. 5, the low-energy photons from dusty torus are the ones dominating the EC contribution. This EC emission has been used in the past to model the broadband emission of BL Lac (Khatoon et al. 2024). In the present flare, owing to the very bright state in which the source was observed during most of the period, we find that the EC emission becomes relevant only at the early stages of the outburst, when the source is faintest (see the model for BB1 in Fig. F.1). We have also considered the possible emission arising from the interplay between the core and blob regions, this is, low-energy photons from one region that can be IC-scattered by electrons of the other region. However, this was found to be negligible due to the compactness of the blob as a result of the size constraints derived from the VHE minute-scale variability. The $\gamma\gamma$ absorption was also evaluated and taken into account, but was found to be negligible up to energies \sim TeV, where the sources is not detected significantly and only upper limits are estimated.

Overall, the parameters are consistent with the typical values derived from a large sample of blazars (Ghisellini et al. 2010). The core region is mainly responsible for the emission from radio to UV wavelengths, and contributes significantly to the hard X-ray emission during those periods in which the X-ray emission is found in the transition from the low- to the high-energy peak of the SED. During the early moments of the flare, when the soft X-rays are also found in the IC peak, it dominates both the soft and hard X-ray emission. Changes in the parameters between adjacent BBs are rather small considering the time interval between consecutive blocks is generally longer than the light crossing time of the core, reflecting its slow evolution. On the other hand, during those periods when BL Lac fully transitions from LSP to ISP and the X-ray emission is entirely produced by synchrotron radiation, the low energy emission of the blob is the one becoming dominant in the X-ray band. We note that the γ_{min} values of the blob are on the high end of normal values. Zech & Lemoine (2021) interpreted these high γ_{min} values in other BL Lac objects as a thermal coupling of protons and electrons in a weakly magnetised shock, where protons transfer energy to electrons in the shock layer.

The main driver of the variability on day-to-week timescales is the evolution of the particle population of each region during the flare. Especially noticeable is the electron distribution behaviour of the blob during the brightest nights (BB4 and BB8), when it clearly reaches higher energies, in consistency with the IC peak shift towards higher energies reported in Sect. 4. Moreover, for these two nights, an injection of freshly accelerated particles was also needed to explain the remarkably high γ -ray emission. The blob is also characterised by a higher magnetisation and higher Doppler boosting than the core, with $B_{blob} = 0.5$ G, $\delta_{blob} = 33$ and $B_{core} = 0.2$ G, $\delta_{core} = 20$, respectively. This, combined with the equipartition values of the core, close to equipartition but still $U'_B/U'_e > 1$, and its sometimes very hard spectral index, are consistent with a magnetic reconnection scenario (see e.g. Jormanainen et al. 2023), discussed in detail in Sect. 6.3. We note that the equipartition values of the blob are far from ~ 1 , with the electron energy density dominating on the order of magnitude of $U'_e \sim 10^2 U'_B$. This is a limitation that is regularly found in these models (see Tavecchio & Ghisellini 2016). This might arise from assuming a still over-simplified picture of the relativistic jets while trying to capture all the observational features, including, week, day and minute scale variability. Nevertheless, the models presented here are able to accurately describe the evolution of the flare while still providing a reason-

able solution to observational features such as multi-wavelength correlations, week-, day- and minute-scale VHE variability.

6.3. Origin of the minute-scale VHE variability

The very fast minute-scale variability demands a compact region with extreme particle acceleration (the blob in our fitting model) on top of the blazar zone (the core in our model) that governs the day-to-week-scale variability. Such a physical setup is often attributed to the mini-jet scenario under magnetic reconnection (Giannios et al. 2009; Petropoulou et al. 2016). A particularly high value of the blob Lorentz factor is also necessary to avoid the VHE γ -ray attenuation in the compact blob. The optical depth for VHE γ -rays is given by $\tau_{\gamma\gamma} \sim (1+z)^2 \sigma_T L_{target} E_{obs} / (72\pi m_e^2 c^6 \delta^6 \tau_{min})$ (Ackermann et al. 2016), where $E_{obs} > 200$ GeV is the observed VHE photon energy, L_{target} is the optical luminosity, which is the target photons for VHE γ -rays, and τ_{min} is the shortest observed variability timescale. We find that the Doppler factor $\delta \gtrsim 30$ can ensure the compact blob is optically thin to the observed VHE photons. This range of Doppler factor values is typically high with respect to those often observed in blazars. Hence, the mini-jet scenario is particularly relevant here to solve this problem and avoid the VHE γ -ray attenuation in the compact blob. Under the mini-jet scenario, the terminal bulk Lorentz factor of the plasmoid can reach approximately the magnetisation factor of the reconnection site in the co-moving frame (Sironi et al. 2016). As shown in Table 3, the magnetisation factor in the core, estimated by U'_B/U'_e , is generally $\gtrsim 1$. The bulk Lorentz factor of the blob relative to the core can be approximated by $\delta_{blob}/\delta_{core}$ (if they are both close to the line of sight), which is comparable to the magnetisation factor. Although our fitting model and the above estimates are rather simplified, they are consistent with the mini-jet in magnetic reconnection scenario (Nalewajko et al. 2011).

A plasmoid merger in magnetic reconnection can be an alternative scenario (Zhang et al. 2022). Previous particle-in-cell (PIC) simulations have shown that the SSC can exhibit much higher and faster variability than the synchrotron and EC, due to the highly concentrated electrons freshly accelerated at the plasmoid merging site. The magnetisation factor therein can drop below 1 even though the reconnection site has overall >1 magnetisation, consistent with the fitting parameters derived for the blob (Zhang et al. 2022). In principle, such collisions and mergers of plasma structures can happen in magnetised turbulence as well (Zhang et al. 2023). However, the very high intrinsic X-ray polarisation ($\sim 49\%$, see Peirson et al. 2023) measured just two days after the last flare disfavors a turbulent environment.

In addition to the fast variability, the very hard particle spectrum in the core ($n_1 \lesssim 2.0$) also indicates a magnetic reconnection origin. Although we fit the radio to optical spectrum by the synchrotron emission from the core, usually the large-scale jet can have a considerable contribution to the radio emission. Therefore, the radio to optical emission intrinsic to the core in our model may require even harder particle spectrum. It is generally believed that only magnetic reconnection in a highly magnetised environment can result in particle spectrum harder than 2 (Guo et al. 2016, 2021). Interestingly, since the correlated quasi-periodic flux and polarisation variations detected by Jorstad et al. (2022) suggested kink instabilities in BL Lac, and the very high optical polarisation degree found in Agudo et al. (2025) indicates the relaxation of a magnetic spring in the jet, with the fast variability reported in the current paper, it is possible that the strong activities of BL Lac since roughly 2020 are associated with gi-

ant eruption of magnetised plasma from the central engine, likely due to the magnetically-arrested-disc jet scenario.

Under this picture, our two-zone model essentially consists of a segment of the kinked jet (the core) and plasmoids (the blob) produced via magnetic reconnection that is triggered by the kinked jet from time to time. Since they are co-spatial and physically connected, all bands above the synchrotron self absorption limit should have some correlations. However, the production of plasmoids and their mergers in reconnection is rather random as shown in numerical simulations (Sironi et al. 2016; Zhang et al. 2022). Hence the VHE emission that is fully dominated by the blob can appear less correlated to the optical emission that is fully dominated by the core. Moreover, the models presented here propose a simplified picture of the magnetic reconnection scenario. As the flare develops, plasmoids grow and can be ejected from the reconnection layer with various physical conditions as suggested by recent PIC simulations (Sironi et al. 2016; Zhang et al. 2024). While a fully numerical treatment of plasma dynamics in reconnection is far beyond the scope of this paper, we model these plasmoids as one blob with highly variable physical parameters as shown in many previous studies (e.g. Christie et al. 2019). We note that the two-zone model has significant parameter degeneracy, thus our fitting parameters may not be unique.

Additionally, we have calculated the blob synchrotron and SSC cooling timescales in the observer frame for the electrons responsible for the GeV-TeV γ -ray emission. The synchrotron cooling timescales were estimated as (see e.g. Abe et al. 2025)

$$t_{sync} = \frac{(1+z)}{\delta_{blob}} \frac{6\pi m_e c}{\sigma_T B^2 \gamma_e}, \quad (8)$$

where m_e is the electron mass, σ_T is the Thomson cross-section, B is the magnetic field of the blob and γ_e is the Lorentz factor of the electrons. The blob SSC cooling timescales in the observer frame were computed as $t_{SSC} = \frac{(1+z)}{\delta_{blob}} \gamma_e / \left(\frac{d\gamma_e}{dt}\right)_{SSC}$, with $\left(\frac{d\gamma_e}{dt}\right)_{SSC}$ expressed in the blob reference frame as (Moderski et al. 2005)

$$\left(\frac{d\gamma_e}{dt}\right)_{SSC} = \frac{4c\sigma_T}{3} \gamma_e^2 \int f_{KN}(4\epsilon\gamma_e) \epsilon n_{ph}(\epsilon) d\epsilon, \quad (9)$$

where ϵ is the photon energy in the rest frame of the blob in units of the electron rest mass energy, $\epsilon = hv'/m_e c^2$, ν' being the photon frequency in the blob frame, f_{KN} is defined by Eq. (C5) in Moderski et al. (2005), $n_{ph}(\epsilon)$ is the synchrotron photon number density in the blob rest frame, computed as in Abe et al. (2025). The blob SSC cooling timescales were found to be shorter than the synchrotron ones, consistent with the Compton dominance of 5–10 shown by the blob SED. In Table 3 we report the blob SSC cooling timescales at $\gamma_e = \gamma_b$. For the two nights with intranight variability, our models predict SSC cooling timescales of the order of few minutes for electrons radiating at GeV-TeV, in agreement with the minute scale variability observed. Therefore, with all the considerations mentioned above, one possible scenario is that the observed flares at VHE γ rays are produced by freshly accelerated particles via magnetic reconnection with a cooling dominated by SSC cooling.

We note that the scenario proposed here is based on a magnetically-dominated region. However, an alternative picture based on a two-zone model with a weakly magnetised plasma can still offer a good fitting to the SED as long as the blob has a higher Lorentz factor than that of the core, and larger than the expected minimum Lorentz factor obtained from the TeV fast variability, estimated above. The most natural way to explain

higher Lorentz factor in a small blob compared to the overall blazar zone is magnetic reconnection. Nevertheless, and owing to the high degeneracy of blazar SED models (as commented in Sect. 5), other combinations of parameters can lead to valid representations of the SED and its evolution, possibly relying on non-magnetically-dominated scenarios.

7. Conclusions

BL Lac has shown one of its three brightest γ -ray and multi-wavelength flares ever between September and November 2023. We have characterised its HE and VHE emission, extending up to a few TeV during the brightest periods of the flare. One of the key features of this event is the significant remarkably fast VHE γ -ray flux variability, with doubling flux timescales as short as 8.3 minutes, which sets tight constraints to the size of the VHE emitting region. This is also among the fastest flux variations ever detected at VHEs from blazars.

The HE-VHE spectrum shows a shift of the peak towards higher energies at the highest stages of the flare. Accompanying this behaviour we also report a softer-when-brighter evolution of the X-ray spectrum due to a clear transition of the X-ray emission from IC-dominated to synchrotron-dominated, meaning that the source also transitions from LSP to ISP, as seen in other periods for BL Lac in the past (Nilsson et al. 2018).

The broadband emission was modelled within a leptonic scenario, motivated by recent results reported by IXPE (Middei et al. 2023; Peirson et al. 2023; Agudo et al. 2025; Liodakis et al. 2025). One-zone models were not successful when trying to explain the broadband emission. Therefore, a co-spatial two-zone SSC model incorporating also the dusty torus EC contribution was used. Within this scenario, the evolution of the jet is driven by changes on the electron population of both regions, with injection of freshly accelerated electrons being the cause of the brightest outbursts. The minute-scale variability observed constrains the size of the compact blob region to be $\lesssim 4.5 \times 10^{14}$ cm for the adopted Doppler factor $\delta_{blob} = 33$, consistent with the value used here. This blob region is therefore the responsible of the intranight γ -ray variability, that can be associated with a plasmoid under a magnetic reconnection event.

References

- Abdollahi, S., Acero, F., Ackermann, M., et al. 2020, *ApJS*, 247, 33
Abe, H., Abe, K., Abe, S., et al. 2023, *ApJ*, 956, 80
Abe, K., Abe, S., Abhir, J., et al. 2025, *A&A*, 697, A172
Abeysekara, A. U., Benbow, W., Bird, R., et al. 2018, *ApJ*, 856, 95
Acero, F., Bernete, J., Biederbeck, N., et al. 2024, *Gammapy v1.2: Python toolbox for gamma-ray astronomy*
Acharyya, A., Agudo, I., Angüner, E. O., et al. 2019, *Astroparticle Physics*, 111, 35
Ackermann, M., Ajello, M., Allafort, A., et al. 2011, *ApJ*, 743, 171
Ackermann, M., Anantua, R., Asano, K., et al. 2016, *ApJ*, 824, L20
Aguasca-Cabot, A., Donath, A., Feijen, K., et al. 2023, *Gammapy: Python toolbox for gamma-ray astronomy*
Agudo, I., Liodakis, I., Otero-Santos, J., et al. 2025, *ApJ*, 985, L15
Agudo, I., Molina, S. N., Gómez, J. L., et al. 2012, in *International Journal of Modern Physics Conference Series*, Vol. 8, *International Journal of Modern Physics Conference Series*, 299–302
Aharonian, F., Akhperjanian, A. G., Bazer-Bachi, A. R., et al. 2007, *ApJ*, 664, L71
Aharonian, F. A. 2000, *New A*, 5, 377
Albert, J., Aliu, E., Anderhub, H., et al. 2007, *ApJ*, 666, L17
Aleksić, J., Ansoldi, S., Antonelli, L. A., et al. 2016, *Astroparticle Physics*, 72, 76
Arlen, T., Aune, T., Beilicke, M., et al. 2013, *ApJ*, 762, 92
Atwood, W. B., Abdo, A. A., Ackermann, M., et al. 2009, *ApJ*, 697, 1071
Ballet, J., Burnett, T. H., Digel, S. W., & Lott, B. 2020, *arXiv e-prints*, arXiv:2005.11208

- Bellm, E. C., Kulkarni, S. R., Graham, M. J., et al. 2019, *PASP*, 131, 018002
- Brown, T. M., Baliber, N., Bianco, F. B., et al. 2013, *PASP*, 125, 1031
- Burrows, D. N. et al. 2005, *Space Sci. Rev.*, 120, 165
- Christie, I. M., Petropoulou, M., Sironi, L., & Giannios, D. 2019, *MNRAS*, 482, 65
- Cleary, K., Lawrence, C. R., Marshall, J. A., Hao, L., & Meier, D. 2007, *ApJ*, 660, 117
- Dermer, C. D. & Schlickeiser, R. 1994, *ApJS*, 90, 945
- Donath, A., Terrier, R., Remy, Q., et al. 2023, *A&A*, 678, A157
- Dondi, L. & Ghisellini, G. 1995, *MNRAS*, 273, 583
- Escudero Pedrosa, J., Agudo, I., Morcuende, D., et al. 2024a, *AJ*, 168, 84
- Escudero Pedrosa, J., Morcuende Parrilla, D., & Otero-Santos, J. 2024b, *IOP4*
- Evans, P. A., Beardmore, A. P., Page, K. L., et al. 2009, *MNRAS*, 397, 1177
- Fitzpatrick, E. L. 1999, *PASP*, 111, 63
- Fomin, V. P., Stepanian, A. A., Lamb, R. C., et al. 1994, *Astroparticle Physics*, 2, 137
- Ghisellini, G. & Tavecchio, F. 2009, *MNRAS*, 397, 985
- Ghisellini, G., Tavecchio, F., Foschini, L., et al. 2010, *MNRAS*, 402, 497
- Giannios, D., Uzdensky, D. A., & Begelman, M. C. 2009, *MNRAS*, 395, L29
- Guo, F., Li, X., Daughton, W., et al. 2021, *ApJ*, 919, 111
- Guo, F., Li, X., Li, H., et al. 2016, *ApJ*, 818, L9
- Henri, G. & Saugé, L. 2006, *ApJ*, 640, 185
- Ho, P. T. P., Moran, J. M., & Lo, K. Y. 2004, *ApJ*, 616, L1
- Jormanainen, J., Hovatta, T., Christie, I. M., et al. 2023, *A&A*, 678, A140
- Jorstad, S. G., Marscher, A. P., Raiteri, C. M., et al. 2022, *Nature*, 609, 265
- Kaspi, S., Brandt, W. N., Maoz, D., et al. 2007, *ApJ*, 659, 997
- Khatoon, R., Böttcher, M., & Prince, R. 2024, *ApJ*, 974, 233
- Kochanek, C. S., Shappee, B. J., Stanek, K. Z., et al. 2017, *PASP*, 129, 104502
- Konigl, A. 1981, *ApJ*, 243, 700
- La Mura, G. 2022, *The Astronomer's Telegram*, 15688, 1
- Li, T. P. & Ma, Y. Q. 1983, *ApJ*, 272, 317
- Liodakis, I., Peirson, A. L., & Romani, R. W. 2019, *ApJ*, 880, 29
- Liodakis, I., Romani, R. W., Filippenko, A. V., et al. 2018, *MNRAS*, 480, 5517
- Liodakis, I., Zhang, H., Boula, S., et al. 2025, *A&A*, 698, L19
- López-Coto, R. et al. 2022, *ASP Conf. Ser.*, 532, 357
- MAGIC Collaboration, Acciari, V. A., Ansoldi, S., et al. 2019, *A&A*, 623, A175
- MAGIC Collaboration, Acciari, V. A., Ansoldi, S., et al. 2020, *A&A*, 638, A14
- Mannheim, K. & Biermann, P. L. 1992, *A&A*, 253, L21
- Maraschi, L., Ghisellini, G., & Celotti, A. 1992, *ApJ*, 397, L5
- Marrone, D. P. & Rao, R. 2008, in *Society of Photo-Optical Instrumentation Engineers (SPIE) Conference Series*, Vol. 7020, Millimeter and Submillimeter Detectors and Instrumentation for Astronomy IV, ed. W. D. Duncan, W. S. Holland, S. Withington, & J. Zmuidzinas, 70202B
- Mattox, J. R., Bertsch, D. L., Chiang, J., et al. 1996, *ApJ*, 461, 396
- Max-Moerbeck, W., Hovatta, T., Richards, J. L., et al. 2014, *MNRAS*, 445, 428
- Middei, R., Liodakis, I., Perri, M., et al. 2023, *ApJ*, 942, L10
- Miller, J. S., French, H. B., & Hawley, S. A. 1978, *ApJ*, 219, L85
- Moderski, R., Sikora, M., Coppi, P. S., & Aharonian, F. 2005, *MNRAS*, 363, 954
- Moralejo, A., Lopez-Coto, R., Vuillaume, T., et al. 2025, *cta-observatory/cta-istchain: v0.10.18 - 2025-02-17*
- Myserlis, I., Agudo, I., Thum, C., et al. 2025, in *Highlights of Spanish Astrophysics XII*, ed. M. Manteiga, F. González-Galindo, A. Labiano-Ortega, M. J. Martínez-González, N. Rea, M. Romero-Gómez, A. Ulla-Miguel, G. Yepes, C. Rodríguez-López, A. Gómez-García, & C. Dafonte, 121
- Nalewajko, K., Giannios, D., Begelman, M. C., Uzdensky, D. A., & Sikora, M. 2011, *MNRAS*, 413, 333
- Nievas Rosillo, M., Acero, F., Otero-Santos, J., et al. 2025, *A&A*, 693, A287
- Nigro, C., Sitarek, J., Gliwny, P., et al. 2023, *agnpy*
- Nigro, C., Sitarek, J., Gliwny, P., et al. 2022, *A&A*, 660, A18
- Nilsson, K., Lindfors, E., Takalo, L. O., et al. 2018, *A&A*, 620, A185
- Norris, J. P., Nemiroff, R. J., Bonnell, J. T., et al. 1996, *ApJ*, 459, 393
- Peirson, A. L., Negro, M., Liodakis, I., et al. 2023, *ApJ*, 948, L25
- Peirson, A. L. & Romani, R. W. 2019, *ApJ*, 885, 76
- Petropoulou, M., Giannios, D., & Sironi, L. 2016, *MNRAS*, 462, 3325
- Poole, T. S., Breeveld, A. A., Page, M. J., et al. 2008, *MNRAS*, 383, 627
- Raiteri, C. M., Villata, M., Capetti, A., et al. 2009, *A&A*, 507, 769
- Raiteri, C. M., Villata, M., D'Ammando, F., et al. 2013, *MNRAS*, 436, 1530
- Roming, P. W. A. et al. 2005, *Space Sci. Rev.*, 120, 95
- Sahakyan, N. & Giommi, P. 2022, *MNRAS*, 513, 4645
- Saldana-Lopez, A., Domínguez, A., Pérez-González, P. G., et al. 2021, *MNRAS*, 507, 5144
- Schlaflly, E. F. & Finkbeiner, D. P. 2011, *ApJ*, 737, 103
- Shappee, B. J., Prieto, J. L., Grupe, D., et al. 2014, *ApJ*, 788, 48
- Sironi, L., Giannios, D., & Petropoulou, M. 2016, *MNRAS*, 462, 48
- Stickel, M., Padovani, P., Urry, C. M., Fried, J. W., & Kuehr, H. 1991, *ApJ*, 374, 431
- Tavecchio, F., Becerra-Gonzalez, J., Ghisellini, G., et al. 2011, *A&A*, 534, A86
- Tavecchio, F. & Ghisellini, G. 2016, *MNRAS*, 456, 2374
- Tavecchio, F., Ghisellini, G., Bonnoli, G., & Ghirlanda, G. 2010, *MNRAS*, 405, L94
- Teraesranta, H., Tornikoski, M., Mujunen, A., et al. 1998, *A&AS*, 132, 305
- Urry, C. M. & Padovani, P. 1995, *PASP*, 107, 803
- Wagner, S. M., Burd, P., Dorner, D., et al. 2022, in *37th International Cosmic Ray Conference*, 868
- Weaver, Z. R., Williamson, K. E., Jorstad, S. G., et al. 2020, *ApJ*, 900, 137
- Wilks, S. S. 1938, *The Annals of Mathematical Statistics*, 9, 60
- Zech, A. & Lemoine, M. 2021, *A&A*, 654, A96
- Zhang, H., Böttcher, M., & Liodakis, I. 2024, *ApJ*, 967, 93
- Zhang, H., Li, X., Giannios, D., et al. 2022, *ApJ*, 924, 90
- Zhang, H., Marscher, A. P., Guo, F., et al. 2023, *ApJ*, 949, 71
- Zhang, Y. H., Celotti, A., Treves, A., et al. 1999, *ApJ*, 527, 719

- ³⁰ INFN Sezione di Bari and Università di Bari, via Orabona 4, 70126 Bari, Italy
- ³¹ Palacky University Olomouc, Faculty of Science, 17. listopadu 1192/12, 771 46 Olomouc, Czech Republic
- ³² Dipartimento di Fisica e Chimica 'E. Segrè' Università degli Studi di Palermo, via delle Scienze, 90128 Palermo, Italy
- ³³ INFN Sezione di Catania, Via S. Sofia 64, 95123 Catania, Italy
- ³⁴ IRFU, CEA, Université Paris-Saclay, Bât 141, 91191 Gif-sur-Yvette, France
- ³⁵ Port d'Informació Científica, Edifici D, Carrer de l'Albareda, 08193 Bellaterra (Cerdanyola del Vallès), Spain
- ³⁶ University of Alcalá UAH, Departamento de Physics and Mathematics, Pza. San Diego, 28801, Alcalá de Henares, Madrid, Spain
- ³⁷ INFN Sezione di Torino, Via P. Giuria 1, 10125 Torino, Italy
- ³⁸ Instituto de Física de Sao Carlos, Universidade de Sao Paulo, Av. Trabalhador Sao-carlense, 400 - CEP 13566-590, Sao Carlos, SP, Brazil
- ³⁹ Department of Physics, TU Dortmund University, Otto-Hahn-Str. 4, 44227 Dortmund, Germany
- ⁴⁰ INFN Sezione di Bari, via Orabona 4, 70125, Bari, Italy
- ⁴¹ University of Rijeka, Department of Physics, Radmile Matejčić 2, 51000 Rijeka, Croatia
- ⁴² Institute for Theoretical Physics and Astrophysics, Universität Würzburg, Campus Hubland Nord, Emil-Fischer-Str. 31, 97074 Würzburg, Germany
- ⁴³ INFN Sezione di Roma La Sapienza, P.le Aldo Moro, 2 - 00185 Rome, Italy
- ⁴⁴ ILANCE, CNRS – University of Tokyo International Research Laboratory, University of Tokyo, 5-1-5 Kashiwa-no-Ha Kashiwa City, Chiba 277-8582, Japan
- ⁴⁵ Physics Program, Graduate School of Advanced Science and Engineering, Hiroshima University, 1-3-1 Kagamiyama, Higashi-Hiroshima City, Hiroshima, 739-8526, Japan
- ⁴⁶ INFN Sezione di Roma Tor Vergata, Via della Ricerca Scientifica 1, 00133 Rome, Italy
- ⁴⁷ University of Split, FESB, R. Boškovića 32, 21000 Split, Croatia
- ⁴⁸ Department of Physics, Yamagata University, 1-4-12 Kojirakawamachi, Yamagata-shi, 990-8560, Japan
- ⁴⁹ Institut für Theoretische Physik, Lehrstuhl IV: Plasma-Astroteilchenphysik, Ruhr-Universität Bochum, Universitätsstraße 150, 44801 Bochum, Germany
- ⁵⁰ Institute of Space Sciences (ICE, CSIC), and Institut d'Estudis Espacials de Catalunya (IEEC), and Institució Catalana de Recerca i Estudis Avançats (ICREA), Campus UAB, Carrer de Can Magrans, s/n 08193 Bellaterra, Spain
- ⁵¹ Sendai College, National Institute of Technology, 4-16-1 Ayashi-Chuo, Aoba-ku, Sendai city, Miyagi 989-3128, Japan
- ⁵² Université Paris Cité, CNRS, Astroparticule et Cosmologie, F-75013 Paris, France
- ⁵³ Josip Juraj Strossmayer University of Osijek, Department of Physics, Trg Ljudevita Gaja 6, 31000 Osijek, Croatia
- ⁵⁴ Chiba University, 1-33, Yayoicho, Inage-ku, Chiba-shi, Chiba, 263-8522 Japan
- ⁵⁵ Kitashirakawa Oiwakecho, Sakyo Ward, Kyoto, 606-8502, Japan
- ⁵⁶ FZU - Institute of Physics of the Czech Academy of Sciences, Na Slovance 1999/2, 182 21 Praha 8, Czech Republic
- ⁵⁷ Astronomical Institute of the Czech Academy of Sciences, Bocni II 1401 - 14100 Prague, Czech Republic
- ⁵⁸ Faculty of Science, Ibaraki University, 2 Chome-1-1 Bunkyo, Mito, Ibaraki 310-0056, Japan
- ⁵⁹ Sorbonne Université, CNRS/IN2P3, Laboratoire de Physique Nucléaire et de Hautes Energies, LPNHE, 4 place Jussieu, 75005 Paris, France
- ⁶⁰ Graduate School of Science and Engineering, Saitama University, 255 Simo-Ohkubo, Sakura-ku, Saitama city, Saitama 338-8570, Japan
- ⁶¹ Institute of Particle and Nuclear Studies, KEK (High Energy Accelerator Research Organization), 1-1 Oho, Tsukuba, 305-0801, Japan
- ⁶² INFN Sezione di Trieste and Università degli Studi di Trieste, Via Valerio 2 I, 34127 Trieste, Italy
- ⁶³ Escuela Politécnica Superior de Jaén, Universidad de Jaén, Campus Las Lagunillas s/n, Edif. A3, 23071 Jaén, Spain
- ⁶⁴ Institute for Nuclear Research and Nuclear Energy, Bulgarian Academy of Sciences, 72 boul. Tsarigradsko chaussee, 1784 Sofia, Bulgaria
- ⁶⁵ Institut de Física d'Altes Energies (IFAE), The Barcelona Institute of Science and Technology, Campus UAB, 08193 Bellaterra (Barcelona), Spain
- ⁶⁶ Grupo de Electronica, Universidad Complutense de Madrid, Av. Complutense s/n, 28040 Madrid, Spain
- ⁶⁷ E.S.CC. Experimentales y Tecnología (Departamento de Biología y Geología, Física y Química Inorgánica) - Universidad Rey Juan Carlos
- ⁶⁸ Macroarea di Scienze MMFFNN, Università di Roma Tor Vergata, Via della Ricerca Scientifica 1, 00133 Rome, Italy
- ⁶⁹ Institute of Space Sciences (ICE, CSIC), Campus UAB, Carrer de Can Magrans, s/n 08193 Bellaterra, Spain
- ⁷⁰ School of Allied Health Sciences, Kitasato University, Sagamihara, Kanagawa 228-8555, Japan
- ⁷¹ RIKEN, Institute of Physical and Chemical Research, 2-1 Hirosawa, Wako, Saitama, 351-0198, Japan
- ⁷² Laboratory for High Energy Physics, École Polytechnique Fédérale, CH-1015 Lausanne, Switzerland
- ⁷³ Charles University, Institute of Particle and Nuclear Physics, V Holešovičkách 2, 180 00 Prague 8, Czech Republic
- ⁷⁴ Institute for Space-Earth Environmental Research, Nagoya University, Chikusa-ku, Nagoya 464-8601, Japan
- ⁷⁵ Kobayashi-Maskawa Institute (KMI) for the Origin of Particles and the Universe, Nagoya University, Chikusa-ku, Nagoya 464-8602, Japan
- ⁷⁶ Graduate School of Technology, Industrial and Social Sciences, Tokushima University, 2-1 Minamijosanjima, Tokushima, 770-8506, Japan
- ⁷⁷ INFN Sezione di Pisa, Edificio C – Polo Fibonacci, Largo Bruno Pontecorvo 3, 56127 Pisa, Italy
- ⁷⁸ Istituto Nazionale di Astrofisica - Osservatorio Astronomico di Capodimonte Via Moiariello 16, 80131 Napoli (Italy)
- ⁷⁹ Gifu University, Faculty of Engineering, 1-1 Yanagido, Gifu 501-1193, Japan
- ⁸⁰ Department of Physical Sciences, Aoyama Gakuin University, Fuchinobe, Sagamihara, Kanagawa, 252-5258, Japan
- ⁸¹ Faculty of Physics and Applied Informatics, University of Lodz, ul. Pomorska 149-153, 90-236 Lodz, Poland
- ⁸² Division of Physics and Astronomy, Graduate School of Science, Kyoto University, Sakyo-ku, Kyoto, 606-8502, Japan
- ⁸³ Dipartimento di Fisica - Università degli Studi di Torino, Via Pietro Giuria 1 - 10125 Torino, Italy
- ⁸⁴ Department of Physics, Konan University, 8-9-1 Okamoto, Higashinada-ku Kobe 658-8501, Japan
- ⁸⁵ Institute for Astrophysical Research, Boston University, 725 Commonwealth Avenue, Boston, MA 02215, USA
- ⁸⁶ Center for Astrophysics | Harvard & Smithsonian, 60 Garden Street, Cambridge, MA 02138 USA
- ⁸⁷ Aalto University Metsähovi Radio Observatory, Metsähovintie 114, 02540 Kylmälä, Finland
- ⁸⁸ Aalto University Department of Electronics and Nanoengineering, P.O. BOX 15500, FI-00076 AALTO, Finland
- ⁸⁹ Institut de Radioastronomie Millimétrique, Avenida Divina Pastora, 7, Local 20, E-18012 Granada, Spain
- ⁹⁰ Max-Planck-Institut für Radioastronomie, Auf dem Hügel 69, D-53121 Bonn, Germany
- ⁹¹ University of Maryland Baltimore County, Baltimore, MD 21250, USA
- ⁹² NASA Goddard Space Flight Center, Greenbelt, MD 20771, USA

Appendix A: Night-wise LST-1 data analysis results

In Table A.1 we compile and summarise the night-wise results of the LST-1 data analysis of BL Lac, that is, the effective observing time after data quality selection, the significance, and the flux of the source above 200 GeV.

Table A.1. Effective observation time, significance and flux level above 200 GeV of BL Lac’s emission for each night of observation.

Day	Observation Time [h]	Significance [σ]	Flux ^a [$\times 10^{-11} \text{ cm}^{-2} \text{ s}^{-1}$]	Day	Observation Time [h]	Significance [σ]	Flux ^a [$\times 10^{-11} \text{ cm}^{-2} \text{ s}^{-1}$]
21/09	1.71	0.32	< 1.2	27/10	1.36	6.48	10.7 ± 1.4
01/10	1.65	1.22	< 2.1	29/10	0.72	6.19	2.9 ± 1.2
03/10	2.86	2.28	1.1 ± 0.5	31/10	1.73	5.08	4.7 ± 0.8
15/10	1.31	7.55	6.5 ± 1.0	01/11	1.35	5.22	2.3 ± 0.7
17/10	2.14	10.77	6.3 ± 0.7	13/11	1.51	30.47	38.7 ± 1.3
18/10	2.48	1.14	< 2.7	15/11	0.76	2.20	8.1 ± 2.7
19/10	2.67	3.26	3.1 ± 1.0	16/11	0.88	0.54	< 6.7
20/10	2.50	48.73	23.8 ± 1.0	17/11	0.87	3.01	5.0 ± 2.4
21/10	1.87	0.70	< 1.6	18/11	1.01	0.68	< 8.3
23/10	1.41	1.70	< 5.1	19/11	0.57	0.66	< 6.6
25/10	2.25	0.13	< 1.9	25/11	0.76	10.53	10.8 ± 1.7
26/10	1.23	4.67	3.3 ± 1.1				

Notes. ^aFor the observations in which the signal has a significance $< 2\sigma$ (TS<4), the 95% confidence level flux upper limits are reported.

Appendix B: X-ray data results

In Table B.1 we report the summary of the results of the *Swift*-XRT analysis, presented in Sect. 2.3. For the observations in which the log-parabola model was preferred over the power-law one with a $\geq 3\sigma$ significance, Table B.2 reports the best-fit parameters of the log-parabola model. The logpar implementation in XSPEC was employed in the fit procedures. The derived SEDs are represented in Fig. B.1, along with those derived from the UVOT analysis in the optical-UV range.

Table B.1. Results of the spectral analysis of the *Swift*-XRT observations of BL Lac during September to November 2022.

Day	MJD	ObsID	Exposure [s]	Significance [σ] Log-parabola model	Flux (0.3 – 10 keV) [$\times 10^{-12} \text{ erg cm}^{-2} \text{ s}^{-1}$]	Flux (2.0 – 10 keV) [$\times 10^{-12} \text{ erg cm}^{-2} \text{ s}^{-1}$]	Spectral index
09/16	59838.6	00014925014	1981	1.7	53 ± 5	24 ± 2	1.81 ± 0.02
09/18	59840.5	00014925015	1994	1.9	19 ± 2	11 ± 1	1.63 ± 0.02
09/20	59842.3	00014925016	572	0.9	26 ± 3	13 ± 3	1.82 ± 0.02
09/23	59845.5	00014925017	705	0.3	24 ± 3	14 ± 2	1.70 ± 0.02
10/17	59869.8	00014925018	1102	1.5	42 ± 3	18 ± 2	2.10 ± 0.02
10/17	59869.9	00014925019	1412	0.4	40 ± 3	18 ± 2	2.00 ± 0.02
10/22	59874.4	00014925021	1978	3.7	77 ± 5	24 ± 3	2.33 ± 0.02
10/23	59875.8	00014925020	1832	4.3	56 ± 5	26 ± 2	1.92 ± 0.02
10/25	59877.0	00014925023	1008	3.8	55 ± 6	27 ± 5	1.82 ± 0.02
10/26	59878.3	00096990012	1034	1.9	37 ± 3	23 ± 2	1.70 ± 0.02
10/29	59881.1	00014925024	1661	3.4	78 ± 5	27 ± 3	2.09 ± 0.02
11/01	59884.1	00014925026	951	1.1	72 ± 3	27 ± 2	2.16 ± 0.02
11/04	59887.3	00014925027	1240	2.3	87 ± 5	32 ± 3	2.22 ± 0.02
11/07	59890.1	00014925028	1035	4.2	60 ± 5	24 ± 3	2.15 ± 0.02
11/12	59895.4	00096990013	849	1.9	219 ± 11	50 ± 3	2.60 ± 0.03
11/13	59896.3	00014925030	1278	2.2	64 ± 3	21 ± 2	2.33 ± 0.02
11/21	59904.8	00014925032	1681	2.4	66 ± 3	26 ± 2	2.14 ± 0.02
11/23	59906.0	00014925033	1447	2.7	124 ± 8	34 ± 3	2.43 ± 0.02
11/25	59908.4	00096990014	865	2.0	93 ± 5	27 ± 2	2.43 ± 0.02
11/25	59908.7	00014925034	2021	2.5	69 ± 6	24 ± 3	2.14 ± 0.02
11/26	59909.5	00096990015	905	2.6	71 ± 6	27 ± 3	2.14 ± 0.02
11/27	59910.2	00096990016	834	2.8	97 ± 15	29 ± 6	2.35 ± 0.02
11/28	59911.9	00089562001	1473	3.7	61 ± 5	24 ± 2	2.09 ± 0.02
11/29	59912.2	00096990017	826	2.7	98 ± 8	31 ± 5	2.33 ± 0.02
11/30	59913.4	00096990018	895	3.7	84 ± 13	47 ± 10	1.82 ± 0.02
12/01	59914.1	00096990019	960	3.2	80 ± 8	32 ± 5	2.09 ± 0.02

Notes. For each observation, the following quantities are reported: day, MJD, *Swift* ObsID, exposure, intrinsic flux reconstructed in the 0.3–10 keV and 2.0–10 keV bands and photon index from the fit assuming a power-law model for the intrinsic source spectrum. For those observations in which the log-parabola model was preferred over the power-law at a significance greater than 3σ , the reported fluxes were reconstructed from the best-fit log-parabola model.

Table B.2. Results of the spectral analyses of *Swift*-XRT data assuming a log-parabola model for the intrinsic spectrum.

Day	MJD	ObsID	Significance [σ] Log-parabola model	E_0 [keV]	α	β	N_0 [$\times 10^{-3} \text{ keV}^{-1} \text{ cm}^{-2} \text{ s}^{-1}$]
10/22	59874.4	00014925021	3.7	1	2.68 ± 0.03	-0.720 ± 0.007	11.7 ± 0.1
10/23	59875.8	00014925020	4.3	1	2.39 ± 0.02	-0.808 ± 0.008	7.3 ± 0.1
10/25	59877.0	00014925023	3.8	1	2.41 ± 0.02	-0.993 ± 0.010	6.2 ± 0.1
10/29	59881.1	00014925024	3.4	1	2.40 ± 0.02	-0.587 ± 0.006	11.2 ± 0.1
11/07	59890.1	00014925028	4.2	1	2.63 ± 0.03	-0.918 ± 0.009	9.1 ± 0.1
11/28	59911.9	00089562001	3.7	1	2.45 ± 0.02	-0.658 ± 0.007	9.0 ± 0.1
11/30	59913.4	00096990018	3.7	1	2.31 ± 0.02	-0.812 ± 0.008	11.6 ± 0.1
12/01	59914.1	00096990019	3.2	1	2.46 ± 0.02	-0.686 ± 0.007	11.6 ± 0.1

Notes. The pivot energy was fixed to $E_0 = 1 \text{ keV}$. Only the observations in which the log-parabola model was preferred over the power-law at a significance greater than 3σ are included in this table. For these observations, the best-fit values of the spectral index α , curvature parameter β and normalisation N_0 are reported.

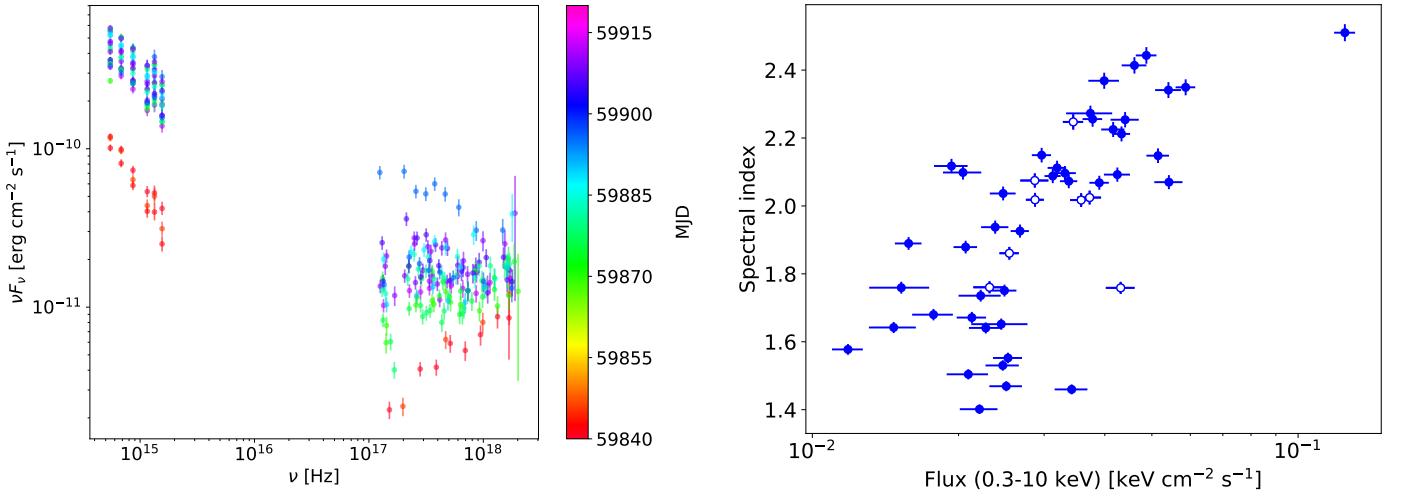


Fig. B.1. Results of the X-ray and UV *Swift* data analysis. *Left:* X-ray and optical-UV SEDs obtained from the *Swift*-XRT/UVOT analyses between September and November 2022. The colour scale corresponds to the MJD of the observation. *Right:* X-ray power-law spectral index as function of the 0.3-10 keV flux. Observations for which a log-parabola shape was preferred over a power law with a significance $\geq 3\sigma$ are shown with open markers.

The right panel of Fig. B.1 shows the scatter plot of the X-ray intrinsic power-law index Γ_X and flux F_X reconstructed from the 50 *Swift*-XRT observations of BL Lac from March 2022 to January 2023 (Sect. 2.3). A softer-when-brighter trend can be highlighted, that is, higher fluxes correspond to softer spectra. The correlation between Γ_X and $\log_{10} F_X$ yields a Pearson coefficient of $\rho = 0.70$, with a p -value under the null hypothesis of non-correlation of $p = 3 \times 10^{-8}$. Hence, a positive correlation is statistically significant. In addition, we observe that the X-ray photon index transitions from values ~ 2.5 , up to ~ 1.4 , indicating a spectrum dominated by the high-energy emission when $\Gamma_X \lesssim 2.0$, and indicating the emergence of an X-ray synchrotron component for $\Gamma_X > 2.0$. The transition is indeed visible in the SED models presented in Sect. 5 and Appendix F, as well as in the left panel of Fig. B.1, where the X-ray spectrum is found in the increasing part of the high-energy SED peak during low emission states, whereas it corresponds to the decreasing part of the synchrotron peak for high-flux periods. For some of the observations, concave log-parabola models were preferred over power-law ones with a significance $\geq 3\sigma$ to describe the intrinsic X-ray spectrum of BL Lac (Table B.2). This indicates that the 0.3 – 10 keV band hosts the valley resulting from the transition between the low-energy and high-energy radiative components (see left panel of Fig. B.1).

Appendix C: *Swift*-UVOT data results

In Table C.1, we report the results of the analyses of *Swift*-UVOT data from the observations carried out from September to November 2022. For each observation, the flux densities in the *Swift*-UVOT photometric bands are reported, corrected for both Galactic extinction and host galaxy contribution (see Sect. 2.4 for more details). The optical-UV SEDs over this period are shown in the left panel of Fig. B.1.

Table C.1. Results of the *Swift*-UVOT photometry of BL Lac in the observations carried out from September to November 2022.

Day	MJD	ObsID	Exposure [s]	V [mJy]	B [mJy]	U [mJy]	W1 [mJy]	M2 [mJy]	W2 [mJy]
09/16	59838.6	00014925014	1948	26.8 ± 1.4	19.5 ± 1.1	12.3 ± 0.8	6.7 ± 0.6	6.2 ± 0.7	4.0 ± 0.4
09/18	59840.5	00014925015	1898	18.8 ± 1.0	13.2 ± 0.8	8.1 ± 0.6	4.6 ± 0.4	3.9 ± 0.4	2.7 ± 0.3
09/20	59842.3	00014925016	547	15.5 ± 1.0	10.5 ± 0.7	6.4 ± 0.5	3.5 ± 0.3	3.0 ± 0.4	1.6 ± 0.2
09/23	59845.5	00014925017	680	18.5 ± 1.1	12.9 ± 0.8	7.0 ± 0.5	3.8 ± 0.4	3.7 ± 0.5	2.0 ± 0.2
10/17	59869.8	00014925018	1450	46.0 ± 2.0	-	-	-	-	-
10/17	59869.9	00014925019	1453	-	-	-	15.5 ± 1.3	-	-
10/22	59874.4	00014925021	1925	99.3 ± 4.7	72.7 ± 3.8	49.6 ± 3.3	28.5 ± 2.4	25.5 ± 2.8	16.2 ± 1.6
10/23	59875.8	00014925020	1758	74.6 ± 3.5	54.3 ± 2.8	36.5 ± 2.4	20.4 ± 1.7	19.5 ± 2.2	12.4 ± 1.2
10/25	59877.0	00014925023	961	63.4 ± 3.0	45.4 ± 2.6	30.0 ± 2.0	16.4 ± 1.4	15.2 ± 1.7	9.5 ± 1.0
10/26	59878.3	00096990012	1009	59.8 ± 2.9	45.0 ± 2.5	29.5 ± 2.0	16.2 ± 1.4	14.4 ± 1.6	9.5 ± 1.0
10/29	59881.1	00014925024	1610	102.1 ± 4.8	72.0 ± 3.7	46.9 ± 3.1	27.5 ± 2.3	25.3 ± 2.8	16.2 ± 1.6
11/01	59884.1	00014925026	928	78.2 ± 3.7	53.8 ± 3.0	34.2 ± 2.3	19.7 ± 1.7	18.5 ± 2.0	12.0 ± 1.2
11/04	59887.2	00014925027	1188	92.9 ± 4.4	65.0 ± 3.6	43.2 ± 2.9	24.4 ± 2.1	22.8 ± 2.5	13.5 ± 1.4
11/07	59890.1	00014925028	990	92.0 ± 4.3	63.8 ± 3.6	44.0 ± 2.9	25.0 ± 2.2	22.8 ± 2.5	14.5 ± 1.5
11/12	59895.4	00096990013	826	97.4 ± 4.6	72.0 ± 4.0	49.6 ± 3.3	29.0 ± 2.5	28.5 ± 3.2	18.3 ± 1.9
11/13	59896.3	00014925030	1254	58.1 ± 2.8	42.9 ± 2.3	29.5 ± 2.0	16.8 ± 1.5	15.8 ± 1.7	10.1 ± 1.0
11/21	59904.8	00014925032	1655	63.4 ± 3.0	45.8 ± 2.4	30.6 ± 2.0	17.0 ± 1.5	16.7 ± 1.8	10.3 ± 1.0
11/23	59906.0	00014925033	1397	83.7 ± 4.0	59.7 ± 3.1	40.1 ± 2.6	22.2 ± 1.9	23.7 ± 2.6	15.0 ± 1.5
11/25	59908.4	00096990014	839	71.8 ± 3.4	50.9 ± 2.9	36.8 ± 2.4	20.6 ± 1.8	19.5 ± 2.2	12.1 ± 1.2
11/25	59908.6	00014925034	1985	61.0 ± 2.9	45.0 ± 2.4	30.9 ± 2.0	17.5 ± 1.5	16.2 ± 1.8	10.4 ± 1.1
11/26	59909.5	00096990015	879	81.3 ± 3.8	58.0 ± 3.3	39.0 ± 2.6	23.0 ± 2.0	21.6 ± 2.4	13.3 ± 1.3
11/27	59910.2	00096990016	809	102.1 ± 4.8	71.4 ± 4.0	48.7 ± 3.2	29.0 ± 2.5	26.4 ± 2.9	17.0 ± 1.7
11/28	59911.9	00089562001	1446	57.0 ± 2.7	40.9 ± 2.2	27.1 ± 1.8	15.1 ± 1.3	14.1 ± 1.6	8.9 ± 0.9
11/29	59912.2	00096990017	801	62.8 ± 3.0	43.7 ± 2.5	29.5 ± 2.0	17.5 ± 1.5	15.6 ± 1.8	9.5 ± 1.0
11/30	59913.4	00096990018	870	69.8 ± 3.3	48.1 ± 2.7	32.3 ± 2.1	18.6 ± 1.6	17.3 ± 1.9	10.6 ± 1.1
12/01	59914.1	00096990019	914	98.3 ± 4.6	68.7 ± 3.9	47.8 ± 3.2	27.5 ± 2.4	25.7 ± 2.8	15.8 ± 1.6

Appendix D: Multi-wavelength light curve analysis

Appendix D.1: Variability

The HE and VHE γ -ray flare studied here and shown in Fig. 1 corresponds to one of the three highest γ -ray activities from this source, together with the roughly equally bright outbursts that occurred on August 2021 and October 2024. The night-wise VHE variability ranges from non-detections during which the emission of the source was low, up to a flux of ~ 1.9 Crab Units (C.U.), a factor ~ 10 with respect to the average emission of 0.23 C.U. over the whole period (see Table A.1 for the night-wise results). This variability becomes even more evident when evaluating the flux on a shorter timescale (see Sect. 3 for more details), reaching a maximum emission of 2.8 C.U. above 200 GeV for the night of November 13, and 4.4 C.U. above 100 GeV for October 20.

Extreme variability is also present in the HE emission of BL Lac, with several rises and decays of the flux over time. The LAT data show an extraordinarily bright period, with the flux changing almost a factor 70 from the minimum to the maximum emission detected, and reaching a flux of $\sim 1.2 \times 10^{-5} \text{ cm}^{-2} \text{ s}^{-1}$ on October 16, being amongst the brightest blazar flares ever detected by this instrument. The LST-1 light curve does not reveal a similar VHE flux increase around October 16, however we note that the LAT light curve is based on a 12-hour binning and the highest state occurs during day time for LST-1, therefore after the VHE γ -ray observations. Hence, we can not exclude the presence of a fast VHE flare such as those observed during October 20 and November 13, with a flux above 200 GeV that significantly increased after the LST-1's observations.

As for the X-ray flux between 0.3 and 10 keV, we observe an energy flux variation of a factor ~ 11 , similar to that in the VHE band, ranging from 22 to 2, in units of $10^{-11} \text{ erg cm}^{-2} \text{ s}^{-1}$. However, we stress that the observing coverage is relatively low especially for the first half of the campaign. Nevertheless, during the second half, the X-ray emission seems to follow the same variability pattern as that seen in HE γ rays. Remarkably, the highest X-ray emission is detected during a period in which the HE γ -ray emission is moderate. Unfortunately, no simultaneous LST-1 observation is available to compare the most energetic γ -ray emission with the high-energy end of the synchrotron component, located in the X-ray band for this observation, see Sect. 5 and Appendix C.

Large variability is also observed in the optical-UV bands. Taking the UVOT *w2* UV band as reference, we measure an average emission of ~ 8.5 mJy, varying a factor 20 between ~ 0.9 and 18.8 mJy. The same increase is measured in the optical *R* band, where the flux density goes from ~ 8.6 mJy at the lowest state, up to ~ 192.9 mJy at the peak of the flare. Finally, as commonly observed for γ -ray blazars, the radio bands show the lowest variability across all bands. At a frequency of 37 GHz, the emission changes from 5.47 and 7.83 Jy, only a factor 1.4, contrasting with the large variability observed at other wavelengths.

Appendix D.2: Correlations

As shown by Fig. 1, the multi-wavelength emission seems to follow similar variability patterns in several bands. In order to quantify the possible correlations between the different bands, we have computed the Spearman's linear correlation coefficient ρ for each

wavelength with respect to the R band. We use strictly simultaneous data within ± 0.1 days to avoid biasing the results as much as possible, with the exception of LAT data, for which we consider the R -band observations within each 12-hour bin.

No significant correlation is observed between the VHE and optical light curves, for which we measure a coefficient $\rho_{R-VHE} = 0.31$ (p -value $p = 0.08$). This contrasts with a mild correlation between the HE and VHE γ -ray bands, that show $\rho_{HE-VHE} = 0.53$ (p -value $p = 0.01$). A very high correlation degree is observed between the optical and UV bands, for which we obtain coefficients $\rho_{R-V} = 0.99$ and $\rho_{R-w2} = 0.98$ (p -values $p = 4.8 \times 10^{-25}$ and $p = 6.3 \times 10^{-22}$), respectively (using the V and $w2$ bands in each case). A high correlation is also observed between the optical and HE γ -ray emission, with $\rho_{R-HE} = 0.79$ (p -value $p = 2.5 \times 10^{-7}$). The X-ray emission on the other hand shows a slightly smaller value, indicating a hint of correlation with the optical emission. The estimated coefficient for this pair of light curves is $\rho_{R-X-ray} = 0.64$ ($p = 4.0 \times 10^{-4}$). We have evaluated the cause of this somewhat lower correlation with respect to the optical-UV bands by calculating the correlation coefficient for the soft (0.3-2 keV) and hard (2-10 keV) X-ray bands. The former shows again a very high degree of correlation with the R band ($\rho_{R-soft} = 0.81$, $p = 6.1 \times 10^{-6}$), whereas the latter shows a lower correlation degree ($\rho_{R-hard} = 0.52$, $p = 0.002$). This can be attributed to the transition of the X-ray emission from the high-energy to the synchrotron SED bump. The hard X-ray band hosts more frequently the valley between both peaks compared to the soft X-ray band (see Appendix C), hence lowering the level of correlation with the optical emission. Finally, the radio emission shows the lowest correlation degree, with $\rho_{R-radio} = 0.41$ ($p = 0.038$). This is not surprising since, as reported in Appendix D.1, the radio emission is the least variable, therefore not following exactly the same variability features as the optical band.

Appendix E: Joint HE-VHE SED fits

In Figs. E.1 and E.2 we show the results of the joint LAT-LST-1 spectral characterisation described in Sect. 4 for all the BBs defined in our analysis. These SEDs correspond to the spectra whose parameters are summarised in Table 2. The spectral shape of the joint analysis at VHE γ -ray energies is also compared with that obtained from an LST-only analysis.

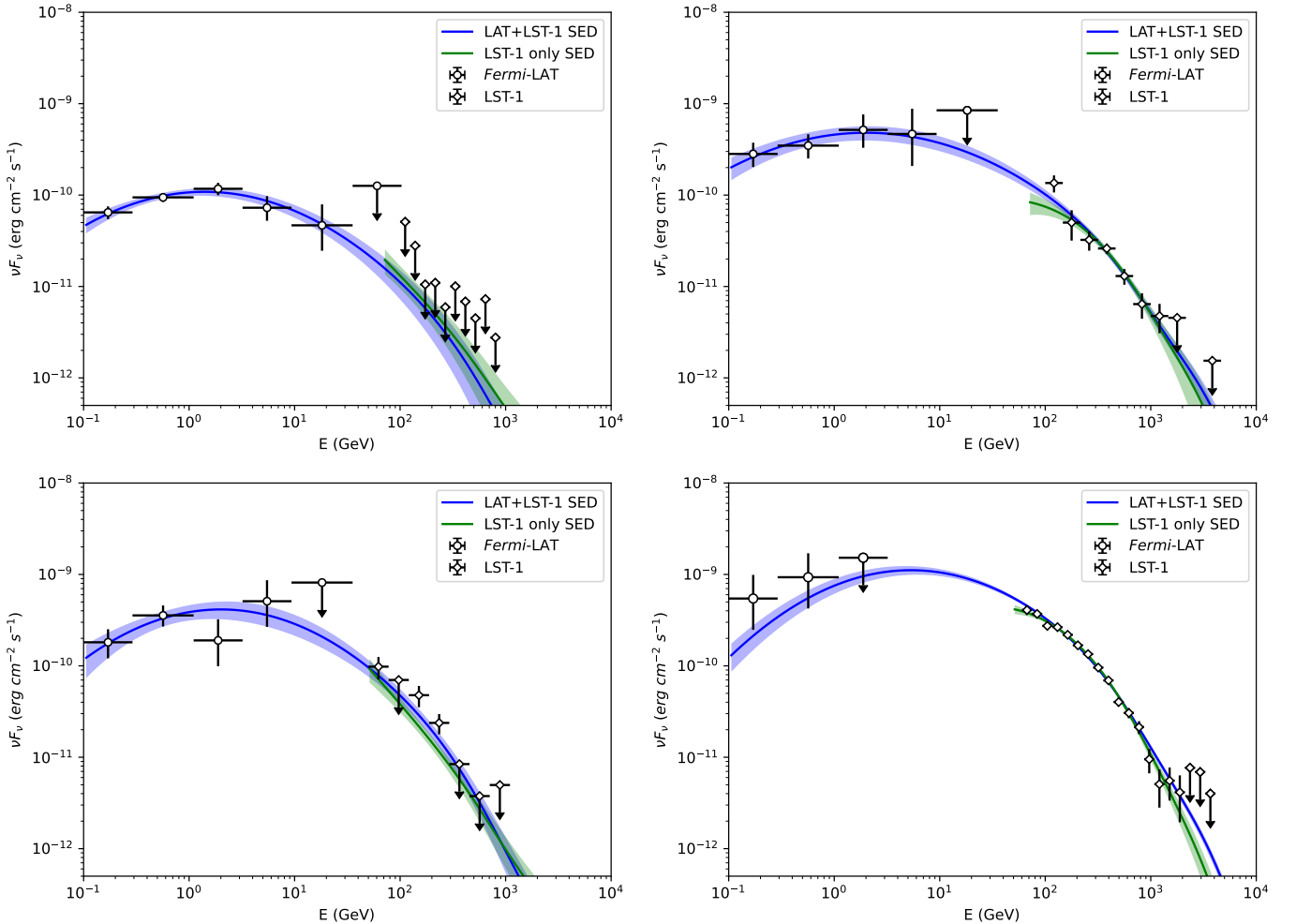


Fig. E.1. Joint LAT-LST-1 SED using a compound log-parabola plus the EBL model from Saldana-Lopez et al. (2021) for BB1 (top left), BB2 (top right), BB3 (bottom left) and BB4 (bottom right). Same description as Fig. 3.

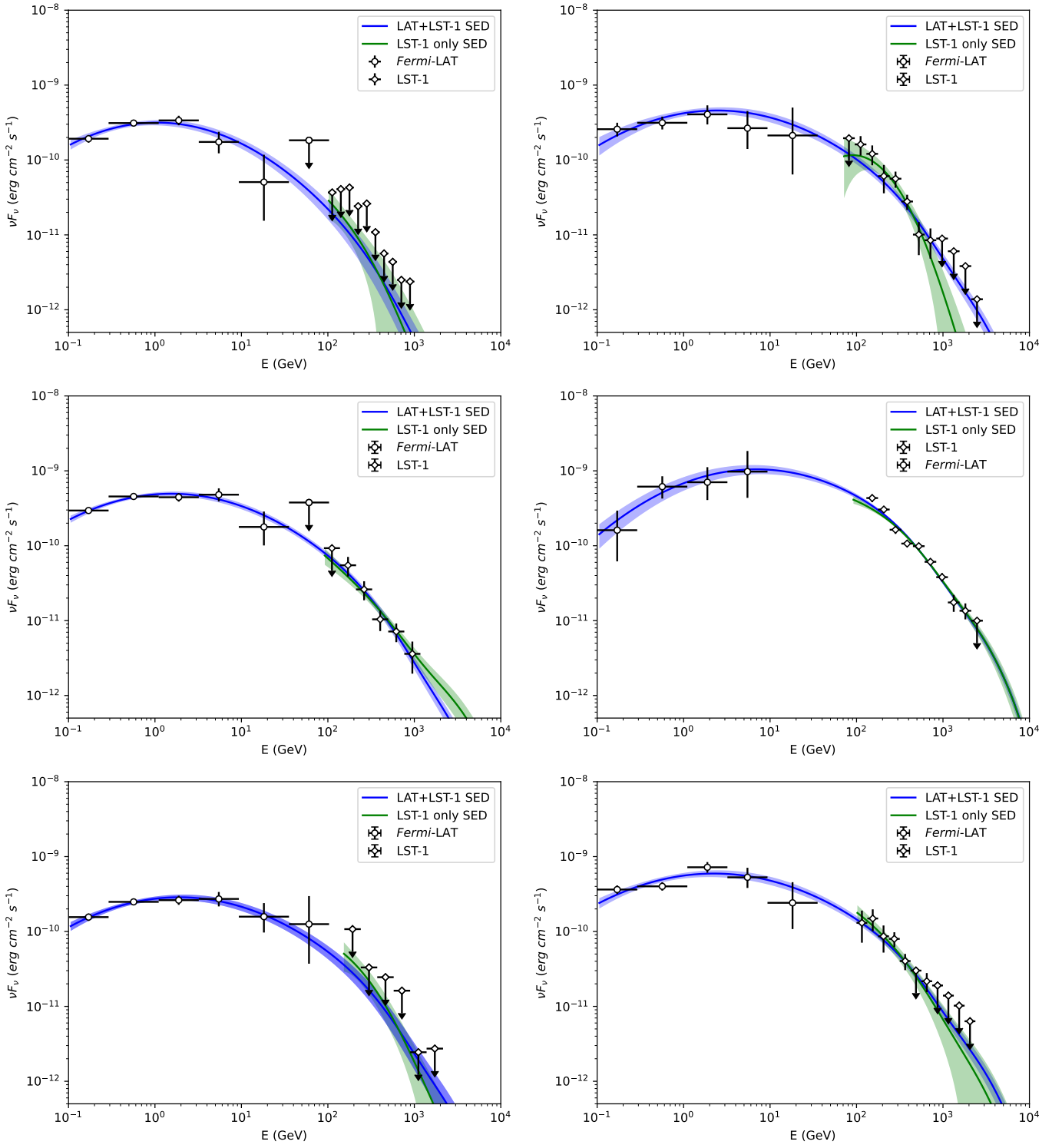


Fig. E.2. Joint LAT-LST-1 SED using a compound log-parabola plus the EBL model from [Saldana-Lopez et al. \(2021\)](#) for BB5 (top left), BB6 (top right), BB7 (middle left), BB8 (middle right), BB9 (bottom left) and BB10 (bottom right). Same description as Fig. 3.

Appendix F: SED models

This appendix gathers the SED models for all 10 BBs defined in Table 2. The fits are represented in Figs. F.1 and F.2, and correspond to the models defined by the parameters reported in Table 3.

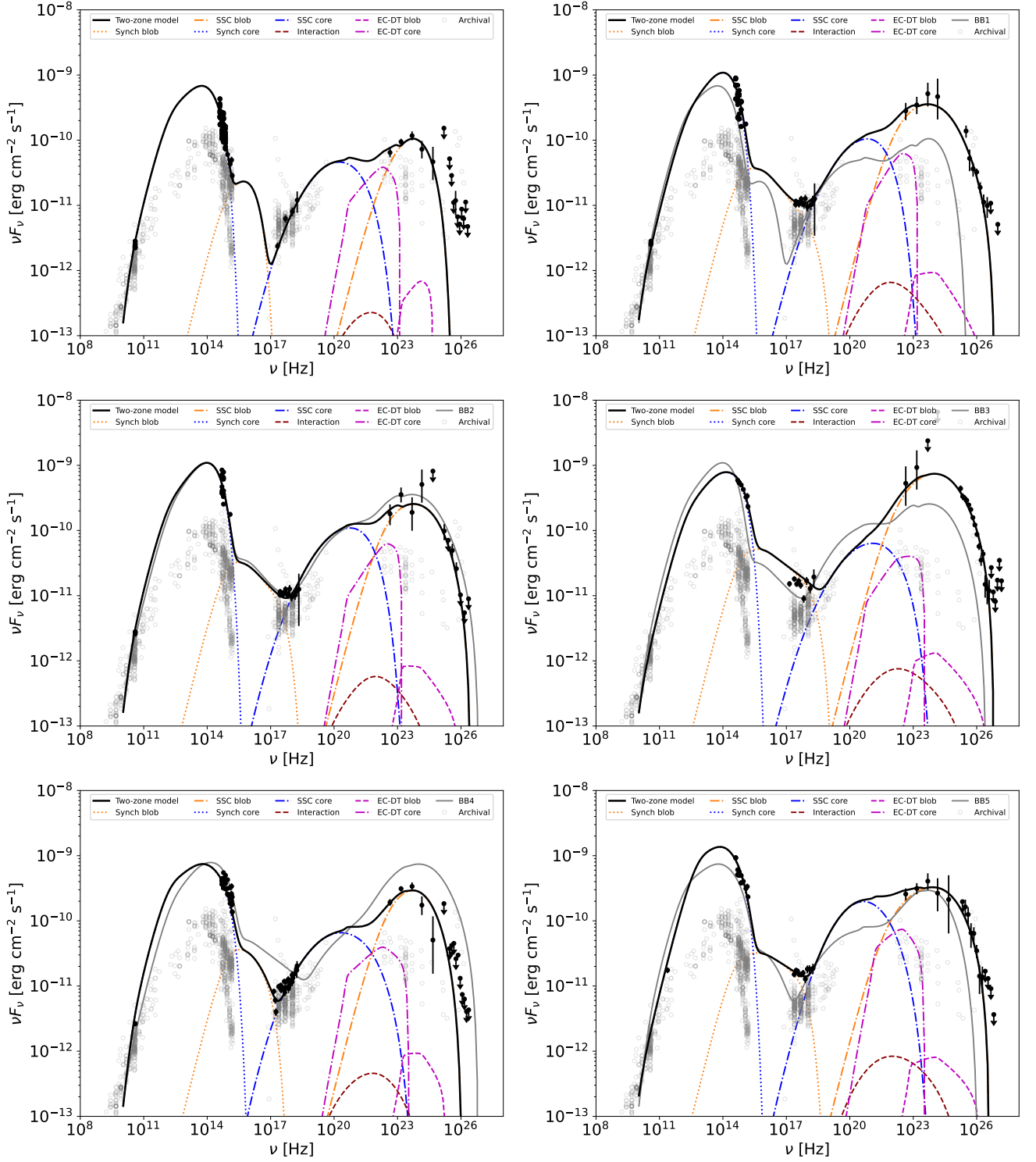


Fig. F.1. Broadband SEDs of BL Lac for BB1 (top left), BB2 (top right), BB3 (middle left), BB4 (middle right), BB5 (bottom left) and BB6 (bottom right). Same description as Fig. 4.

139117NB-C43, PID2022-139117NB-C44, PID2022-136828NB-C42, PID2024-155316NB-I00, PDC2023-145839-I00 funded by the Spanish MCIN/AEI/10.13039/501100011033 and by ERDF/EU and NextGenerationEU PRTR; CSIC PIE 202350E189; the "Centro de Excelencia Severo Ochoa" program through grants no. CEX2020-001007-S, CEX2021-001131-S, CEX2024-001442-S; the "Unidad de Excelencia María de Maeztu" program through grants no. CEX2019-000918-M, CEX2020-001058-M; the "Ramón y Cajal" program through grants RYC2021-032991-I funded by MICIN/AEI/10.13039/501100011033 and the European Union "NextGenerationEU"/PRTR and RYC2020-028639-I; the "Juan de la Cierva-Incorporación" program through grant no. IJC2019-040315-I and "Juan de la Cierva-formación" through grant JDC2022-049705-I; the "Viera y Clavijo" postdoctoral program of Universidad de La Laguna, funded by the Agencia Canaria de Investigación, Innovación y Sociedad de la Información. They also acknowledge the "Atracción de Talento" program of Comunidad de Madrid through grant no. 2019-T2/TIC-12900; "MAD4SPACE: Desarrollo de tecnologías habilitadoras para estudios del espacio en la Comunidad de Madrid" (TEC-2024/TEC-182) project, Doctorado Industrial (IND2024/TIC34250) and Ayudas para la contratación de personal investigador predoctoral en formación (PIPF-2023/TEC-29694) funded by Comunidad de Madrid; the La Caixa Banking Foundation, grant no. LCF/BQ/PI21/11830030; Junta de Andalucía under Plan Complementario de I+D+I (Ref. AST22_0001) and Plan Andaluz de Investigación, Desarrollo e Innovación as research group FQM-322; Project ref. AST22_00001_9 with funding from NextGenerationEU funds; the "Ministerio de Ciencia, Innovación y Universidades" and its "Plan de Recuperación, Transformación y Resiliencia"; "Consejería de Universidad, Investigación e Innovación" of the regional government of Andalucía and "Consejo Superior de Investigaciones Científicas", Grant CNS2023-144504 funded by MICIU/AEI/10.13039/501100011033 and by the European Union NextGenerationEU/PRTR, the European Union's Recovery and Resilience Facility-Next Generation, in the framework of the General Invitation of the Spanish Government's public business entity Red.es to participate in talent attraction and retention programmes within Investment 4 of Component 19 of the Recovery, Transformation and Resilience Plan; Junta de Andalucía under Plan Complementario de I+D+I (Ref. AST22_00001), Plan Andaluz de Investigación, Desarrollo e Innovación (Ref. FQM-322). "Programa Operativo de Crecimiento Inteligente" FEDER 2014-2020 (Ref. ESFRI-2017-IAC-12), Ministerio de Ciencia e Innovación, 15% co-financed by Consejería de Economía, Industria, Comercio y Conocimiento del Gobierno de Canarias; the "CERCA" program and the grants 2021SGR00426 and 2021SGR00679, all funded by the Generalitat de Catalunya; and the European Union's NextGenerationEU (PRTR-C17.11). This work is funded/Co-funded by the European Union (ERC, MicroStars, 101076533). This research used the computing and storage resources provided by the Port d'Informació Científica (PIC) data center. State Secretariat for Education, Research and Innovation (SERI) and Swiss National Science Foundation (SNSF), Switzerland; The research leading to these results has received funding from the European Union's Seventh Framework Programme (FP7/2007-2013) under grant agreements No 262053 and No 317446; This project is receiving funding from the European Union's Horizon 2020 research and innovation programs under agreement No 676134; ESCAPE - The European Science Cluster of Astronomy & Particle Physics ESFRI Research Infrastructures has received funding from the European Union's Horizon 2020 research and innovation programme under Grant Agreement no. 824064. H.Z. is supported by NASA under award number 80GSFC24M0006. Some of the data are based on observations collected at the Observatorio de Sierra Nevada; which is owned and operated by the Instituto de Astrofísica de Andalucía (IAA-CSIC). This article is based on observations made with the IAC80 operated on the island of Tenerife by the Instituto de Astrofísica de Canarias in the Spanish Observatorio del Teide. This work makes use of observations from the Las Cumbres Observatory global telescope network. This work makes use of data from the All-Sky Automated Survey for Supernovae (ASAS-SN). This work has made use of data from the Joan Oró Telescope (TJO) of the Montsec Observatory (OdM), which is owned by the Catalan Government and operated by the Institute for Space Studies of Catalonia (IEEC). Based on observations obtained with the Samuel Oschin Telescope 48-inch and the 60-inch Telescope at the Palomar Observatory as part of the Zwicky Transient Facility project. ZTF is supported by the National Science Foundation under Grants No. AST-1440341 and AST-2034437 and a collaboration including current partners Caltech, IPAC, the Oskar Klein Center at Stockholm University, the University of Maryland, University of California, Berkeley, the University of Wisconsin at Milwaukee, University of Warwick, Ruhr University, Cornell University, Northwestern University and Drexel University. Operations are conducted by COO, IPAC, and UW. This publication makes use of data obtained at the Metsähovi Radio Observatory, operated by the Aalto University. The Submillimeter Array is a joint project between the Smithsonian Astrophysical Observatory and the Academia Sinica Institute of Astronomy and Astrophysics and is funded by the Smithsonian Institution and the Academia Sinica. Maunakea, the location of the SMA, is a culturally important site for the indigenous Hawaiian people; we are privileged to study the cosmos from its summit.

Author contributions: D. Cerasole: *Swift*-XRT/UVOT data analysis, SED modelling and discussion, paper edition. G. Emery: LST-1 data analysis, systematic evaluation, paper edition. D. Morcuende: LST-1 data analysis, paper edition. J. Otero-Santos: project coordination, LST-1, *Fermi*-LAT and multi-wavelength data analysis, SED modelling and interpretation, paper edition. H. Zhang: theoretical interpretation, paper edition. The rest of the authors have contributed in one or several of the following ways: design, construction, maintenance and operation of the instrument(s) used to acquire the data; preparation and/or evaluation of the observation proposals; data acquisition, processing, calibration and/or reduction; production of analysis tools and/or related Monte Carlo simulations; discussion and approval of the contents of the draft.